Research Papers

Theoretical investigation of an enhanced multiphase change energy storage material for buildings

Rizal Sinaga [a,b,*], Jo Darkwa [a], Siddig Omer [a], Mark Worall [a]

[a] Buildings, Energy and Environment Research Group, The Faculty of Engineering, The University of Nottingham, University Park, Nottingham NG7 2RD, UK
[b] Metallurgical Engineering Study Program, Institut Teknologi Del, Laguboti, Toba Samosir 22381, Indonesia

ARTICLE INFO

ABSTRACT

Recent developments have highlighted the potential of multiphase change materials (MCM) as flexible energy storage materials for application in buildings. The MCM was obtained by combining the microencapsulated heptadecane (MEHept) and microencapsulated octacosane (MEOct) using polymelamine formaldehyde (PMF) as the shell material. For the purpose of enhancing thermal performance of MEHept, MEOct, and MCM, different amounts of graphene were included as a thermal conductivity additive. Results indicated the thermal performance improvement of MEHept and MEOct by 39 % and 62 %, respectively, compared to samples without graphene. Analysis of the theoretical results also achieved about 34 % enhancement in thermal conductivity of MCM with an optimum 5 wt% of graphene but resulted in 21 % reduction in energy storage capacity. Despite the study has demonstrated the possibility of using graphene to increase the thermal properties of MCM, deeper experimental work is strongly recommended to align it with the simulation results.

1. Introduction

Thermal energy plays a crucial role in the overall energy consumption across various global locations and exerts a notable impact on greenhouse gas emissions [1]. The buildings sector represents almost 40 % of the overall worldwide energy usage, mostly allocated for space heating/cooling and hot water supplies [2]. Hence, there is a requirement for energy-efficient technologies to reduce energy usage and mitigate greenhouse gas emissions in the building industry.

Phase change materials (PCMs) have been identified as potential thermal energy storage (TES) materials that can be used to minimise energy consumption in buildings [3–5]. For example, Darkwa [6] and Zhou et al. [7] achieved up to 30 % reduction in heating and cooling loads with a composite PCM plasterboard system. Kishore et al. [8] examined the performance of a PCM wall and observed a decrease in annual heat gain by 15 % to 72 % and a reduction in heat loss ranging between 7 % and 38 %.

The PCMs require encapsulation to protect their thermophysical and structural integrity, especially during the phase transition. Several studies [9–11] have conducted extensive study on the use of microencapsulated PCM (MEPCM) in building applications by utilising polymer shell materials. Most of the MEPCMs were integrated into building materials to provide a comfortable indoor temperature during various seasons in the range of 5 °C until 80 °C [12]. Among various types of PCMs, n-heptadecane and n-octacosane have been identified experimentally as the core materials for MEPCMs in numerous studies [13–17], attributed to their appropriate melting temperature at 22 °C and 61 °C and relatively high energy storage capacity [18].

Nevertheless, commercially available MEPCMs have relatively low thermal conductivities [19] and fixed phase transition temperatures and thus constraining their adaptability for multiple seasonal applications in buildings [20]. As a result, several investigations such as Ma et al. [21–23] and Su et al. [24] have been conducted in an effort to overcome those barriers but with limited success. Sinaga et al. [25] and Su et al. [26] however managed to combine two MEPCMs to obtain a multiphase change material (MCM) with multiple melting temperatures, but still possesses low thermal conductivity. Fundamental understanding of the enhancing mechanism is therefore essential for the development of the MCM and establishment of technological advantage.

Nevertheless, it is not entirely practicable to understand the behaviour of the microstructure experimentally. Therefore, theoretical investigation through molecular dynamic (MD) simulation would be a

---

useful tool for studying the thermal behaviour of the MCM at molecular level. Basically, MD simulation is a computational method for predicting the movement of particles over time based on Newton's equation of motion, by associating with potential or force field of the molecules [27].

Researchers have shown that MD simulation is capable of predicting the thermophysical properties of composite micro/nano-encapsulated PCM. For example, Rao et al. [28] studied the melting behaviour of nanoencapsulated PCM with constrained and free shells employing inorganic silica (SiO_2) shell to encapsulate n-octadecane. When the shell was constrained, the energy associated with the harmonic restraint was at its lowest point in terms of distance or angle. It was reported the melting temperature of system with free and constrained shell were respectively at 303 K and 313 K. Furthermore, they determined that the constrained shell confined the PCM molecules, hence reducing their mobility and resulting in a lowered diffusion coefficient. Nevertheless, the use of a free and soft shell led to the improved thermal performance for energy storage.

Despite the recent increase in the number of published studies, the quantity of research conducted in MD simulation for MEPCM remains significantly low [29], let alone MCM system. Particularly, when the organic polymer shell was used as the shell material. The construction of MEPCM with organic shell material would be more complicated due to the huge number of atoms as the addition of long-chain polymer shell materials [30]. For example, Liu et al. [30] constructed the model by combining n-octacosanoic, n-dosane, and polystrene shell material. Due to the long-chain polymer, the polystrene structure was simplified and combined randomly with the core materials. The phase change temperature of mixture was found in temperature range of 363 K – 383 K, which was higher than those of pure n-docosane and n-octacosanoic at 317 K and 335 K, respectively. Due to the introduction of polystrene, the thermal conductivity of the mixture was 0.158 W/m K. This value was lower than those of pure PCMs at 0.22 W/m K and 0.170 W/m K for n-docosane and n-octacosanoic, respectively. Zhang et al. [31] introduced graphene into ethylene–vinyl acetate (EVA) and n-pentacosane composites. The graphene was added with a proportion of 0.7 wt% up to 7.0 wt% separately. It was indicated that the sample containing 0.7 wt% graphene exhibited the greatest values compared to all other samples. The thermal conductivity was calculated to be within the range of 0.4331 W/m K to 0.4086 W/m K over a temperature range of 313 K to 353 K. Ding et al. [32] studied the thermophysical properties of EVA-encapsulated PCM with the addition of double-walled carbon nanotube (DWNT). The n-pentacosane was selected as the PCM, and DWNT was included in amounts of 4.9–17.1 wt%. The findings indicated that the composite with 13.4 wt% DWNT demonstrated the maximum thermal conductivity, exhibiting a 15 % enhancement compared to the composite without DWNT. However, when the DWNT approached to 17.1 wt% and even 20.5 wt%, the simulated thermal conductivity declined considerably lower than that without DWNT.

The literature review indicates a lack of studies on the theoretical analysis of the development and enhancement of MCM. Additionally, the aforementioned investigations have clearly elucidated the key factors that influence the effective advancement of improved micro/nano-encapsulated PCM. Carbon-based material, such as graphene, is extensively employed as thermal conductivity enhancer due to their non-corrosive properties, lightness, and relatively low density [33]. However, the inclusion of additives may adversely affect the characteristics of the composite PCM [34]. Therefore, this research aims to theoretically analyse the development of MCM using n-heptadecane and n-octacosane as PCMs, and to determine the optimum quantity of graphene to enhance thermal performance of MCM.

2. Theoretical modelling

2.1. Simulation methodology

2.1.1. Force field function

Chemistry at Harvard Macromolecular Mechanics (CHARMM) [35] force field (FF) was selected as the force field in this simulation. The functional forms of CHARMM FF are formulated as in Eqs. (1)–(6). Tersoff potential [36] was utilised to represent the atom interaction of graphene when it was introduced to MEPCMs. Large-scale Atomic/Molecular Massively Parallel Simulator (LAMMPS) [37] software was carried out for the MD simulations.

$$E = \sum_{bonds} k_b(b - b_0)^2 + \sum_{angles} k_\theta(\theta - \theta_0)^2 + \sum_{U-B} k_{UB}(s - s_0)^2$$
$$+ \sum_{dihedrals} k_\varnothing[1 + cos(n\varnothing - \delta)] + \sum_{improper} k_\omega(\omega - \omega_0)^2 + \sum_{non-bond} E_{vdw} + E_{coul}$$

$$(1)$$

where k_b, k_θ, k_{UB}, $k_\varnothing$, and k_ω are the bond, angle, Urey-Bradley (U—B), dihedral, and improper force constants. Variables b, θ, s, $\varnothing$ and ω are the bond length between atoms, bond angle, Urey-Bradley 1,3-distance, dihedral angle, and improper angle respectively. The "0" subscript represents the equilibrium state. Variable n in the dihedral term denotes periodicity with δ; its phase. Variable r_{ij} is the distance between two non-bonded pair of atoms i and j. The non-bonded energy consists of Lennard Jones (LJ) and Columbic interactions with additional switching functions that ramp the energy and/or force smoothly to zero between an inner and outer cut-off as shown in the following formula as $S(r)$.

$$E_{vdw} = \begin{cases} LJ(r), r < r_{in} \\ S(r) \times LJ(r), r_{in} < r < r_{out} \\ 0, r > r_{out} \end{cases} \quad (2)$$

$$E_{coul} = \begin{cases} C(r), r < r_{in} \\ S(r) \times C(r), r_{in} < r < r_{out} \\ 0, r > r_{out} \end{cases} \quad (3)$$

$$LJ(r) = 4\varepsilon \left[\left(\frac{\sigma}{r}\right)^{12} - \left(\frac{\sigma}{r}\right)^6 \right] \quad (4)$$

$$C(r) = \frac{Cq_i q_j}{\varepsilon r} \quad (5)$$

$$S(r) = \frac{\left[r_{out}^2 - r^2\right]^2 \left[r_{out}^2 + 2r^2 - 3r_{in}^2\right]}{r_{out}^2 - r_{in}^2} \quad (6)$$

Variable q, σ, and ε represent the atomic partial charge, distance at the LJ minimum, and LJ well depth, accordingly. In this simulation, r_{in} and r_{out} were respectively set to 10 Å and 12 Å.

The interaction parameters between atoms were obtained by the Lorentz-Berthelot mixing rules [38]:

$$\varepsilon_{ij} = \left(\varepsilon_{ii}\varepsilon_{jj}\right)^{1/2}, \sigma_{ij} = \frac{1}{2}\left(\sigma_{ii} + \sigma_{jj}\right) \quad (7)$$

2.1.2. Mean square displacement

Mean square displacement (MSD) is the statistical average of particle trajectories with time that can characterise the diffusion behaviour of all particles [39], as formulated in Eq. (8).

$$MSD = \frac{1}{N} \left\langle |r_i(t) - r_i(0)|^2 \right\rangle \quad (8)$$

where N denotes the quantity of atoms, $r_i(t)$ and $r_i(0)$ refer to the position of ith atom as the function of time t.

2.1.3. Self-diffusion coefficient

Self-diffusion is a thermophysical property that contributes to char-

acterise mass transport events and provides the microscopic design of materials. [30,40]. In brief, the diffusion coefficient is a parameter that quantifies the level of atomic mobility and motion. The self-diffusion is expressed as in Eq. (9).

$$D = \frac{1}{6N} \lim_{t \to \infty} \frac{d}{dt} \sum_{t=1}^{N} \left\langle |r_i(t) - r_i(0)|^2 \right\rangle \tag{9}$$

In comparison to Eq. (8), the determination of the self-diffusion coefficient involves the calculation of the gradient of the MSD.

2.1.4. Radial distribution function (RDF)

RDF, $g(r)$, is a mathematical representation that describes the change of atoms density as a function of their distance from a certain atom [41]. In other words, the term RDF refers to the chance of identifying an atom inside the infinitesimal volume element dr, situated at a distance r from a specified atom [42]. The RDF is formulated as in Eq. (10).

$$x_\alpha x_\beta \rho g_{\alpha\beta}(r) = \frac{1}{N} \left\langle \sum_{i=1}^{N_\alpha} \sum_{j=1}^{N_\beta} \delta(r - r_i - r_j) \right\rangle \tag{10}$$

where x_α and x_β denote the mole fraction of chemical type α and β, respectively. The variable ρ indicates the overall number density. Variables N_α and N_β are the number of atoms corresponding to chemical type α and β, respectively.

2.1.5. Non-equilibrium molecular dynamic (NEMD) method

In this study, non-equilibrium molecular dynamic (NEMD) method was chosen to compute thermal conductivity. Basically, thermal conductivity (κ) is defined as the amount of the thermal energy that flows per unit time through a unit area with a temperature gradient, as formulated by Fourier's law in Eq. (11).

$$\kappa_x = \frac{J_x}{dT/dx} \tag{11}$$

where J_x and dT/dx respectively represent the heat flux and temperature gradient along the x-direction. The heat flux is formulated as the amount

of heat energy (Q) which flows per unit time (t) across the cross-sectional area (A) perpendicular to the transport direction. Due to the periodicity of box condition, twice of area is involved and resulting in the thermal conductivity formula as in Eq. (12).

$$\kappa_x = \frac{dQ/dt}{2A\left(dT/dx\right)} \tag{12}$$

As mentioned by Chavan et al. [43], the thermal performance of a system was influenced by the change in orientation. Hence, the thermal conductivity calculation in this simulation was computed in the x, y, and z axes.

2.2. Model structure

The model structure for heptadecane ($C_{17}H_{36}$) is shown in Fig. 1(a) where it was randomly duplicated to construct amorphous 200 molecules of heptadecane in a box of simulation system of 50 Å × 50 Å × 50 Å. Meanwhile, Fig. 1(b) displays the octacosane ($C_{28}H_{58}$) with duplicated 123 molecules in a simulation box of 60 Å × 60 Å × 60 Å. Due to the packed nature of the molecules, about 10,600 and 10,578 of atoms were obtained for the amorphous heptadecane and octacosane, respectively.

By considering previous studies [30,31] about the long-chain polymer, the structure of PMF in this study is simplified. According to the schematic reaction shown in Reference [44, 45] the simplified PMF model structure is displayed in Fig. 2.

The force field parameters were initially generated by CHARMM General Force Field (CGenFF) [46] version 3.0.1. Unfortunately, the penalties of parameter and charge are higher than 100, which indicates poor analogy and mandate extensive optimisation. Therefore, missing parameters were identified by using Force Field Toolkit (ffTK) [47] to scan existing parameter files and ORCA [48] was utilised for calculation at the quantum mechanical (QM) level of theory.

As mentioned by Su et al. [26], the multiphase change material (MCM) was obtained by merging MEPCMs with different melting temperature. Therefore, the structure of MCM in MD simulation was

(a)

(b)
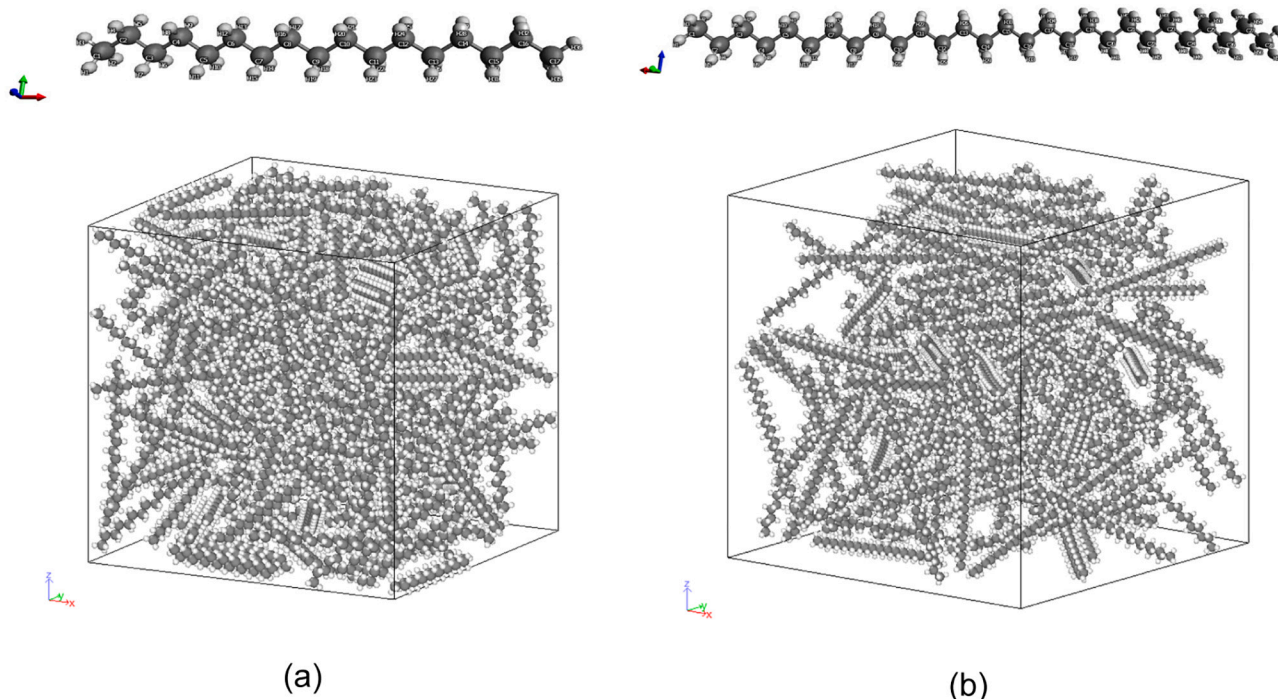
Fig. 1. Initial amorphous structure of (a) heptadecane, and (b) octacosane.
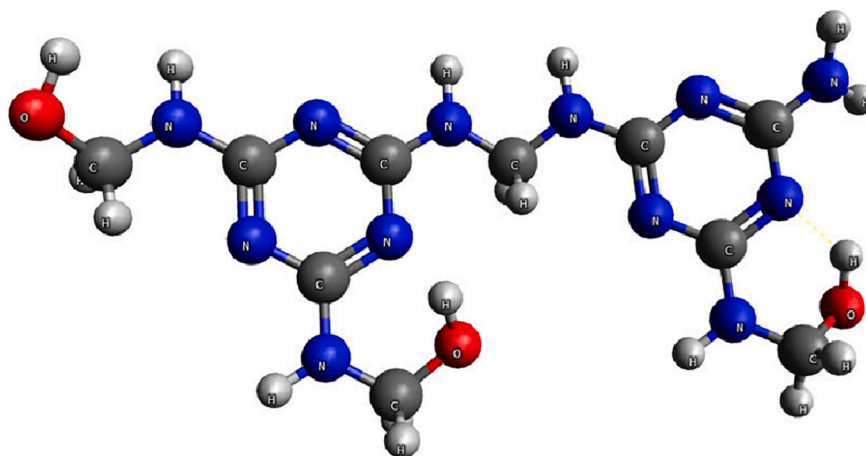
Fig. 2. Simplified PMF shell structure.

developed by combining MEHept and MEOct in a simulation box. For the purpose of enhancing the MCM, graphene was initially combined at various compositions in MEPCMs by fixing it in the centre of the structure. Subsequently, the potential MEPCMs were selected to achieve the enhanced MCM. Fig. 3 shows the model structures of the composite samples where graphene was added to the MEHept and MEOct at various concentrations as listed in Table 1.

3. Results and discussions

3.1. Heptadecane and microencapsulated heptadecane (MEHept)

3.1.1. Pure heptadecane

During the simulation, the periodic boundary condition (PBC) was used at all directions of the box. The simulation was configured as real

unit with time step of 0.5 femtosecond (fs), and the pressure was set at atmospheric pressure. Conjugate gradient algorithm was adopted in the simulation during minimisation to avoid the instability of initial structure [49]. According to the results reported by Lin and Rao [50], the surge of potential curve for amorphous phase was not clearly shown during the heating process for the aim of melting investigation. In contrast, perfect crystal resulted in a distinct characteristic during phase transition.

Therefore, the amorphous phase of heptadecane (Fig. 1(a)) was heated at fixed temperature and pressure (NPT) ensemble from 245 K to 365 K at rate of 2 K/ns. The temperature was controlled by the Nose-Hoover [51] thermostat, and the Nose-Hoover [52] barostat was adopted to prevent pressure drift. Subsequently, the 200 molecules of heptadecane were cooled down from 365 K to 245 K to obtain the crystalline structure, as depicted in Fig. 4.

(a)

(b)

(c)
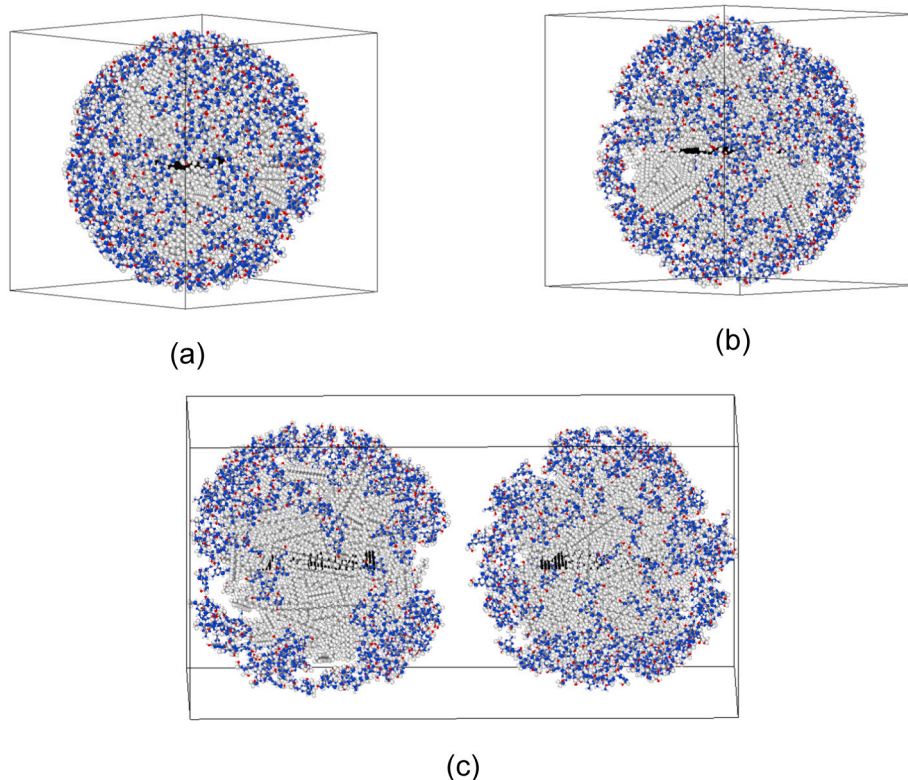
Fig. 3. Model structure of (a) MEHept, (b) MEOct, and (c) MCM.

Table 1
Graphene in MEPCMs.

Sample (MEHept-XGr/MEOct-XGr)	Graphene content (%)	Number of atoms of graphene	Graphene size (Å²)
MEHept-0Gr/MEOct-0Gr	0	0	0
MEHept-0.5Gr/MEOct-0.5Gr	0.5	48	9 × 12
MEHept-1Gr/MEOct-1Gr	1	112	15 × 16
MEHept-2Gr/MEOct-2Gr	2	200	23 × 20
MEHept-3Gr/MEOct-3Gr	3	308	27 × 27
MEHept-5Gr/MEOct-5Gr	5	544	40 × 30
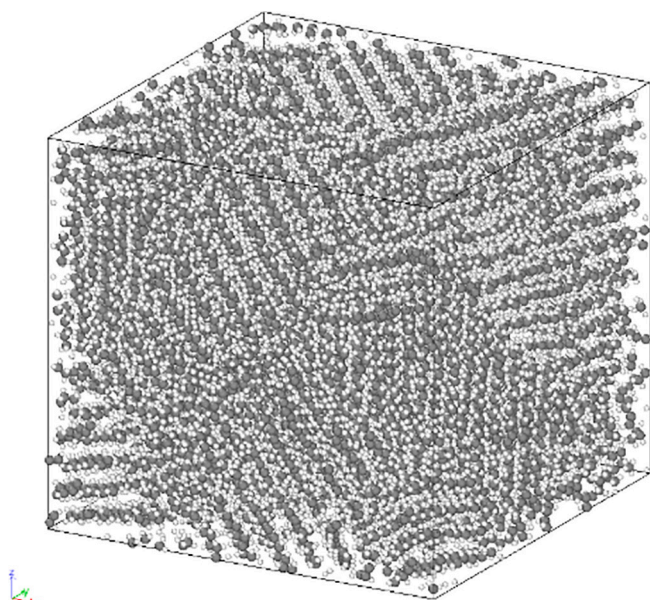
Fig. 4. Crystalline structure of heptadecane.

The density profile during the cooling process of heptadecane is presented in Fig. 5(a). It is clearly shown a surge gradient at temperature range of 290 until 310 K, which indicates the phase transition from liquid to solid. The result revealed a solidification temperature of around 294.5 K, with a corresponding density of approximately 0.79 g/cm³, which is very identical to the value reported by Su et al. [18] as 0.77 g/cm³. The solidification temperature is also found identical at 21.30 °C (294.45 K), as reported by Sari et al. [14].

The enthalpy profile of solidified heptadecane was obtained as in Fig. 5(b). The enthalpy change that occurred during the phase transition was used to calculate the latent heat (Δh) of solidification. The value was about 2353.17 kCal/mol, which is equivalent to 204.71 J/g and slightly lower than what Sari et al. [14] obtained as 213.96 J/g.

Fig. 6(a) illustrates a positive correlation between the temperature of heptadecane and the growth rate of MSD. As the temperature of heptadecane increases, the growth rate of MSD also increases. The observed trend in the MSD curve for heptadecane indicated a notable increase in slope, exhibiting a more pronounced inclination at temperatures equal to or over 295 K. Based on the density and enthalpy profiles depicted in Fig. 5, it can be observed that the phase transition occurred at around 294 K, which closely aligns with the patterns exhibited by the MSD profile. Fig. 6(b) depicts the temperature dependence of the self-diffusion coefficient for the simulated heptadecane structure. The simulated data shows that the self-diffusion coefficient of heptadecane exhibited a

(a)

(b)
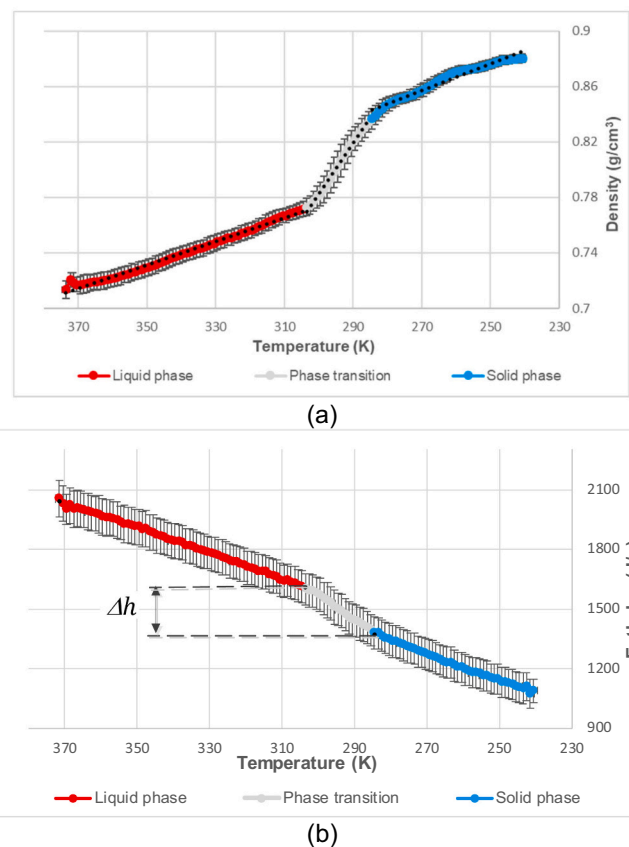
Fig. 5. The averaged (a) density and (b) enthalpy profile of pure heptadecane during crystallisation.

rise with the temperature increase. The intersection between two linear regressions indicates a phase transition, which is resulted by the structural deformation of heptadecane during melting process. Therefore, the intersection lines observed in Fig. 6(b) shows the phase transition temperature of heptadecane to be about 295–300 K.

Fig. 7 represents the RDF profile of pure heptadecane within temperature range of 245 K and 345 K. As the temperature rises, the RDF peak gets weaker, implying a decrease in the ordered structure of heptadecane. This change in pattern agrees with the concept of phase transition.

Thermal conductivity of heptadecane was carried out by dividing the entire system into 100 slabs in x, y, and z directions, as illustrated in Fig. 8. NEMD involves the imposition of a temperature gradient within the system, followed by the computation of generated heat flux [53]. Therefore, a heated plate was positioned at one-fourth of the length, as indicated by the red block. The heat sink, shown as a blue block, was positioned within the cold slabs, occupying three-quarters of the length of the system. Finally, the thermal conductivity can be determined by using the Fourier law, as shown in Eq. (12).

The thermal conductivity of heptadecane at 298 K was determined by maintaining the hot and cold regions at 318 K and 278 K, respectively. The model was initially equilibrated in the constant energy and volume (NVE) ensemble, followed by thermal conductivity calculation for 1,000,000 steps using 0.5 fs of time step. For the calculation of heat flux, it is required to account for the amount of heat energy which flows per unit time across the cross-sectional area perpendicular to the transport direction. The heat flow was determined by calculating the translational kinetic energy for each atom in the system on a per-atom level. The relationship between this energy and the length of time of the simulation is illustrated in Fig. 9(a) at x axes. It is noticeable that both relationships exhibit linearity. The average heat flow can be
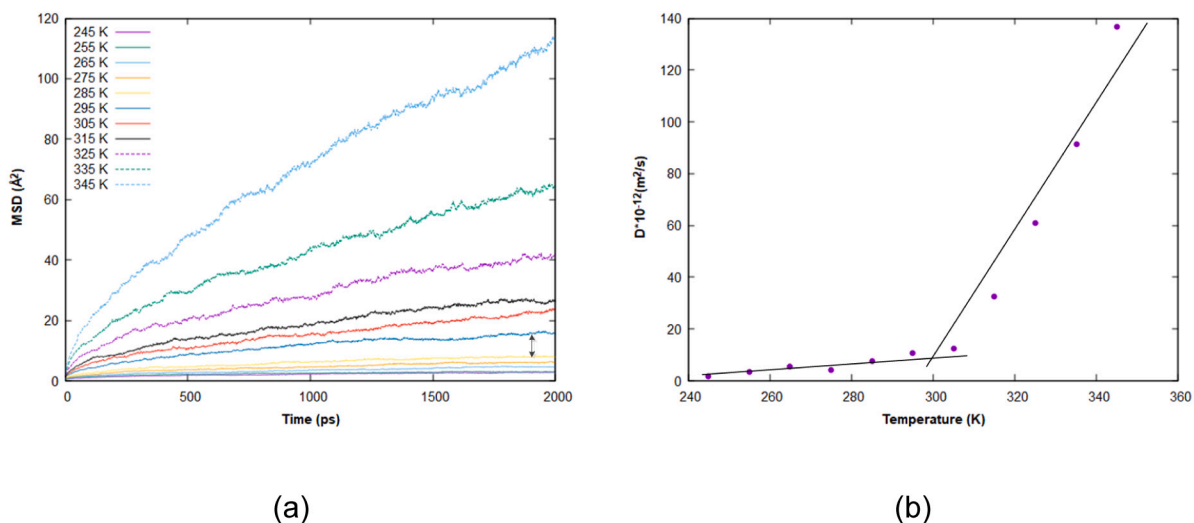
Fig. 6. Simulated (a) MSD and (b) diffusion coefficient of pure heptadecane.
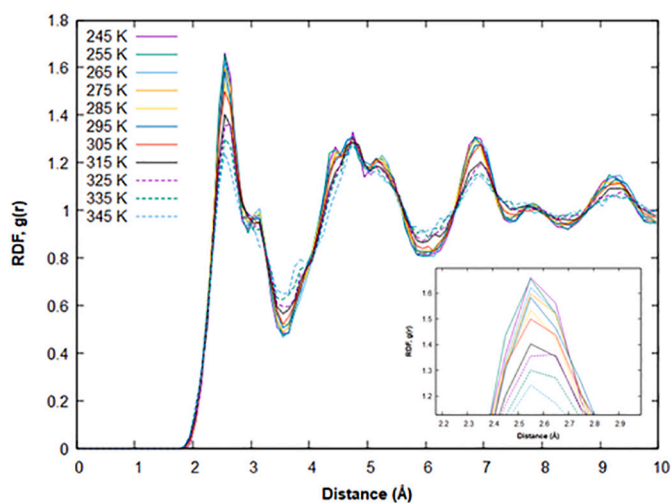
Fig. 7. The RDF of pure heptadecane.

determined by analysing the gradients of the fitted function, resulting in values of about 0.024 kCal/mol fs, 0.029 kCal/mol fs, and 0.027 kCal/mol fs in the x, y, and z-direction, respectively.

Subsequently, the temperature gradient was computed based on the temperature profile, which is plotted and then modelled using two linear functions. Due to the PBC, the fitting is performed individually in the expanded regions indicated in Fig. 9(b) along the x direction. The average temperature gradients in these regions were then obtained as 1.753 K/Å, 1.792 K/Å, and 1.739 K/Å at x, y, and z axes, accordingly.

The computed thermal conductivities were then found by 0.232 W/m·K, 0.270 W/m·K, and 0.258 W/m·K, respectively. Finally, by calculating the average value, the thermal conductivity is obtained as 0.253 W/m·K at 298 K. Thermal conductivities of heptadecane at various temperatures in x, y, and z directions were subsequently calculated and presented in Table 2.

The thermal conductivities were then compared to experimental value reported by Vélez et al. [54], as shown in Fig. 10. The calculated thermal conductivity is about 1.41 until 1.77 higher than the reported values. In addition, both computed and reference values demonstrate a consistent pattern, indicating that thermal conductivity declines with increasing temperature.
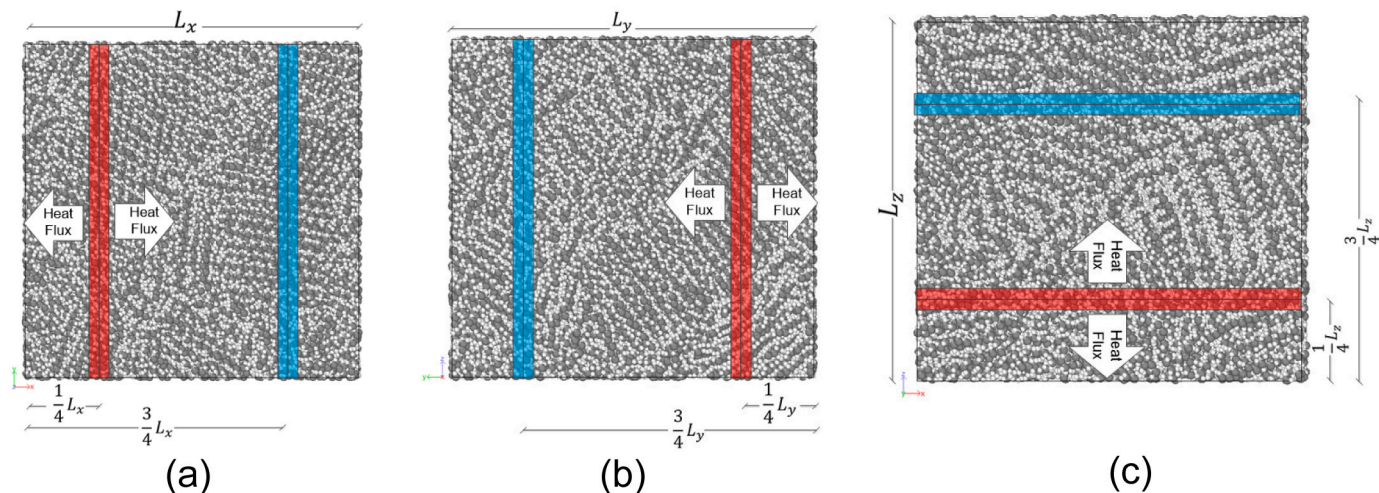
Fig. 8. Schematic diagram of heptadecane for thermal conductivity calculation in (a) x, (b) y, and (c) z direction

(a)

(b)
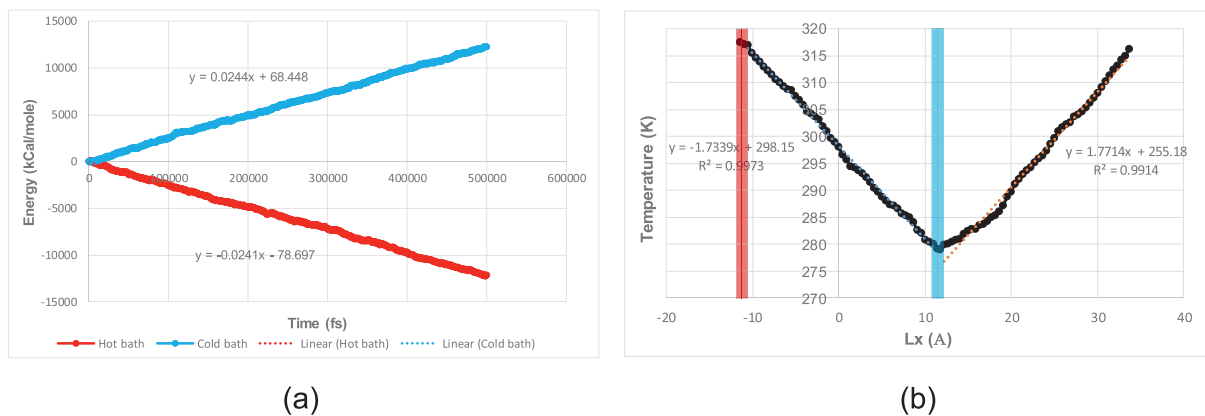
Fig. 9. The (a) energy and (b) temperature gradient of pure heptadecane in *x* direction at 298 K.

Table 2
Thermal conductivity of pure heptadecane in *x*, *y*, and *z* directions at various temperatures.

Temperature [K]	κ (W/m·K)			
	κ_x	κ_y	κ_z	κ_{ave}
245	0.257	0.311	0.268	0.279 ± 0.029
275	0.240	0.312	0.268	0.273 ± 0.036
298	0.232	0.270	0.258	0.253 ± 0.019
315	0.211	0.289	0.263	0.255 ± 0.040
345	0.219	0.223	0.243	0.228 ± 0.013
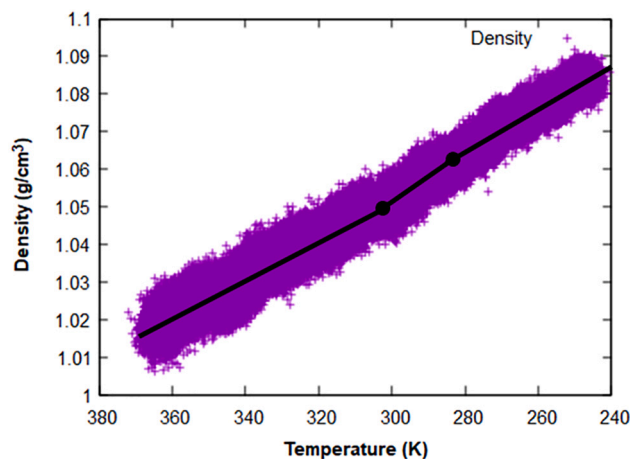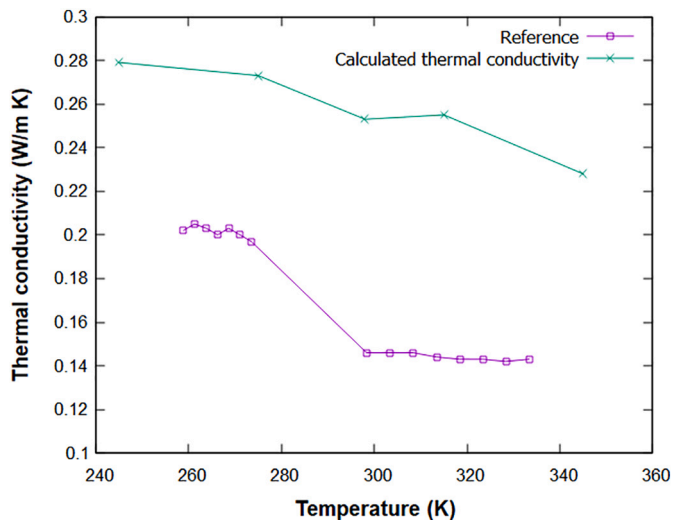
Fig. 10. The calculated thermal conductivity of pure heptadecane at different temperature and the value in Reference [54].

3.1.2. Microencapsulated heptadecane (MEHept)

Similar to the pure heptadecane, the MEHept system was initially minimised. Next, the system was heated from 245 K to 365 K at NPT ensemble at rate of 2 K/ns. The system was subsequently cooled down from 365 K to 245 K at 2 K/ns.

The density profile of MEHept was recorded and exhibited in Fig. 11. Based on the density profiles, the phase transition phenomenon of MEHept was not as distinct as in pure heptadecane. However, different slope in the range of 284.5 K until 304.5 K was found in the density profile, indicating a phase change region. The average temperature at which this phase transition occurs is 294.5 K.

For further phase transition investigation, MSD and self-diffusion coefficient were analysed. Fig. 12(a) shows the MSD of MEHept for

Fig. 11. The density profile of MEHept.

temperature 245 K until 345 K. The MSD has a positive correlation with both temperature and simulation time in general. Furthermore, as the temperature increases, the development rate of MSD accelerates. As can been seen in Fig. 12(a), it clearly illustrates that the phase change temperature of MEHept starts from 285 K, as indicated by the sudden change in the slope of the curve. Furthermore, the self-diffusion coefficient in Fig. 12(b) shows clearly the phase transition at about 294 K, which is consistent with the density profile.

Self-diffusion coefficient of MEHept is exhibited in Fig. 12(b). The self-diffusion intensity of MEHept was found lower than that in pure heptadecane in Fig. 6(b). The self-diffusion coefficient of pure heptadecane is seen from $1.83 \times 10^{-12} m^2/s$ to $136.83 \times 10^{-12} m^2/s$. On the other hand, the diffusion coefficient of MEHept is very low, varying between $1.17 \times 10^{-12} m^2/s$ to $29 \times 10^{-12} m^2/s$. This suggests that the PMF shell is likely responsible for controlling the diffusion of MEHept. Thus, it may be inferred that the thermal conductivity of MEHept is expected to be lower than that of pure heptadecane. Additionally, the varying diffusion abilities of the different components in the mixture demonstrate that the PMF chains in MEHept will hinder the movement of the heptadecane molecules.

The energy storage capacity was then calculated based on the enthalpy profile as presented in Fig. 13. Unlike pure heptadecane, the phase transition of MEHept is not clearly shown in enthalpy profile. A potential issue occurs from the PMF shell material, which may limit volumetric thermal expansion during the phase change of PCM [31]. However, according to the density profile and self-diffusion coefficient, it can be obtained that the energy storage of MEHept during phase
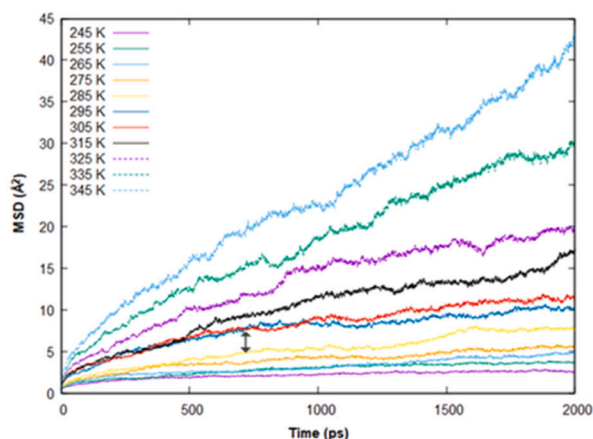
(a)
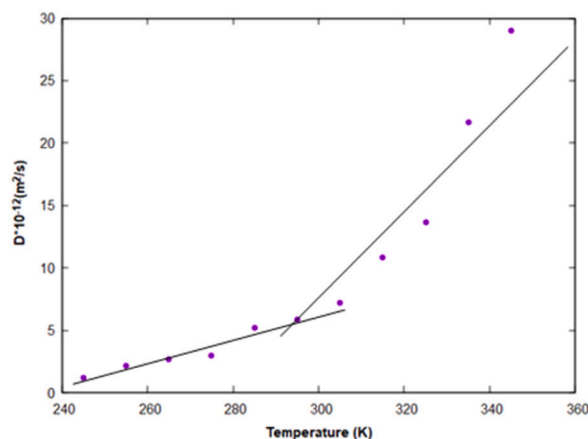
(b)

Fig. 12. The simulated (a) MSD and (b) self-diffusion coefficient of MEHept.
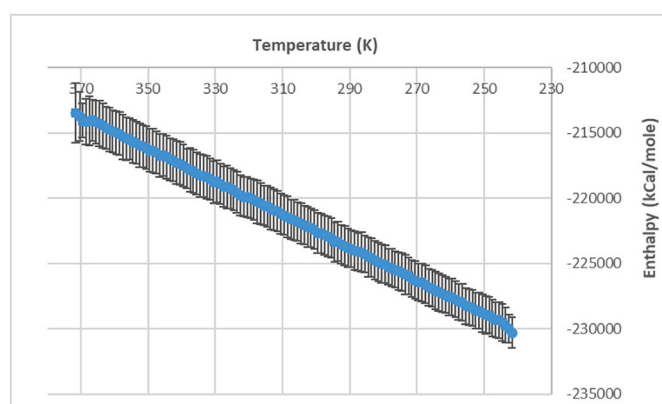
Fig. 13. The enthalpy profile of MEHept.

transition range of 284.5–304.5 K is 2238.59 kCal/mol. This value is about 95.13 % of that pure heptadecane.

Fig. 14 illustrates the RDF of MEHept, indicating a decline in peak intensity as the temperature rises from 245 K to 345 K. The main peak was detected at 2.65 Å, which exhibits a lower magnitude compared to
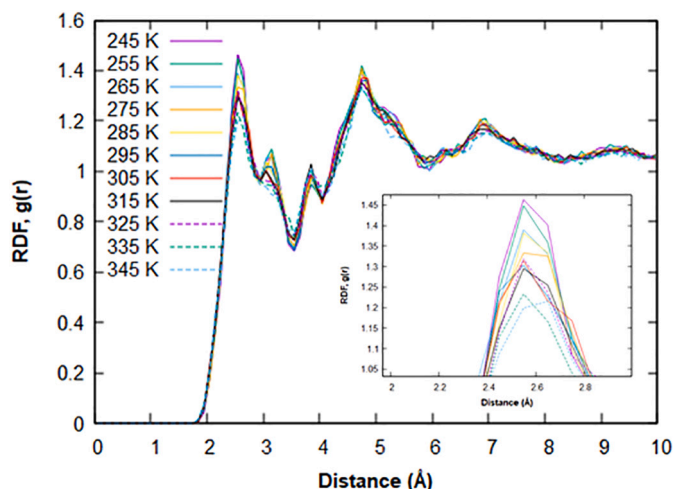
Fig. 14. The RDF of MEHept.

that of pure heptadecane. This suggests that the PMF shell restricted the movement of core material molecules. In addition, the weakened appearance of the major peaks of the MEHept is less significant compared to the pure heptadecane, which confirms the reduction of heat performance, as also reported by Liu et al. [30] due to the addition of polystyrene to n-docosane and n-octacosanoic. As a result, the PMF shell material could slow down the transfer of heat in the MEHept, leading to lower thermal conductivity compared to pure heptadecane.

The phase transition of composite MEHept samples can be seen from the density profile, as depicted in Fig. A-1. It is obvious that the phase transition of most composite MEHept took place between 285 K and 315 K, which exhibited a phase transition similar to that of pure heptadecane and MEHept.

The simulated MSD and self-diffusion coefficient of composite MEHept samples are displayed in Fig. A-2 and Fig. A-3, respectively. However, in comparison with pure heptadecane, most of composite MEHept had a lower maximum MSD value and self-diffusion coefficient due to the restriction of shell material.

The latent heat of composite MEHept was calculated based on the profiles depicted in Fig. A-4. The phase transition temperatures and energy storage capacities of pure heptadecane and all MEHept samples are then summarised in Table 3.

It is obvious that the phase transition temperatures of most composite MEHept were observed slightly different than that of pure heptadecane. On the other hand, the energy storage declines with the increasing of graphene in the composite MEHept. Encapsulation efficiency was defined as the ratio of the latent heat of the MEHept to that of pure heptadecane. It was then found the gradual decrease of encapsulation efficiency from 90.25 % to 73.35 % when 0.5 wt% until 5 wt% of graphene was introduced to the MEHept.

The RDF profiles of all composite MEHept samples are presented in Fig. A-5. Similar to MEHept, all main peaks were observed at a distance of about 2.65 Å, 4.75 Å, 6.55 Å, and 9.25 Å. With the rise in graphene content in MEHept, the primary peaks show tendency to rise, indicating the potential for enhanced thermal conductivity.

By also utilising NEMD method, the thermal conductivity of MEHept was computed at x, y, and z directions. The average heat flux of MEHept at x axes was obtained as 0.032 kcal/mol fs, as shown in Fig. 15(a), while the average value at y and z directions were 0.033 kcal/mol fs and 0.035 kcal/mol fs, respectively. It was subsequently computed the average temperature gradient of MEHept at 298 K at x direction, as shown in Fig. 15(b), by about 1.445 K/Å, while at y and z directions were 1.395 K/Å, and 1.409 K/Å, accordingly. Then the thermal conductivity of

Table 3
Thermophysical properties of pure heptadecane and MEHept samples.

Sample	Phase transition		Encapsulation Efficiency (%)	$\kappa_{ave\ (W/m\cdot K)}$	
	Temperature (K)	Enthalpy (kCal/mol)		$T = 245$ K	$T = 298$ K
Pure Heptadecane	294.50	2353.17	–	0.279 ± 0.028	0.253 ± 0.019
MEHept	294.50	2238.59	95.13	0.232 ± 0.011	0.237 ± 0.011
MEHept-0.5Gr	304.51	2123.74	90.25	0.236 ± 0.009	0.227 ± 0.016
MEHept-1Gr	297.01	2000.19	85.00	0.219 ± 0.009	0.233 ± 0.007
MEHept-2Gr	294.99	1835.69	78.17	0.234 ± 0.019	0.229 ± 0.020
MEHept-3Gr	293.51	1815.67	77.16	0.242 ± 0.038	0.235 ± 0.035
MEHept-5Gr	300.50	1726.14	73.35	0.334 ± 0.150	0.330 ± 0.140

(a)

(b)
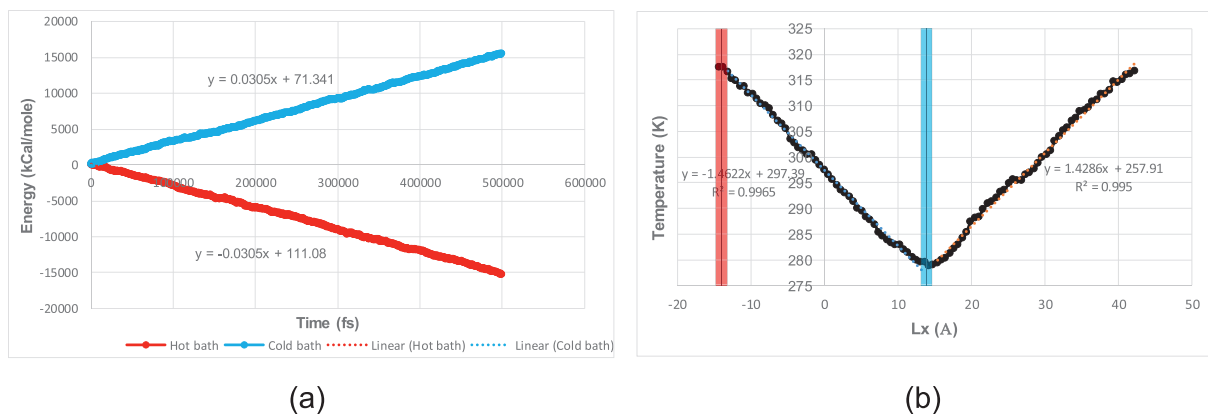
Fig. 15. The (a) energy and (b) temperature gradient of MEHept in *x* direction at 298 K.
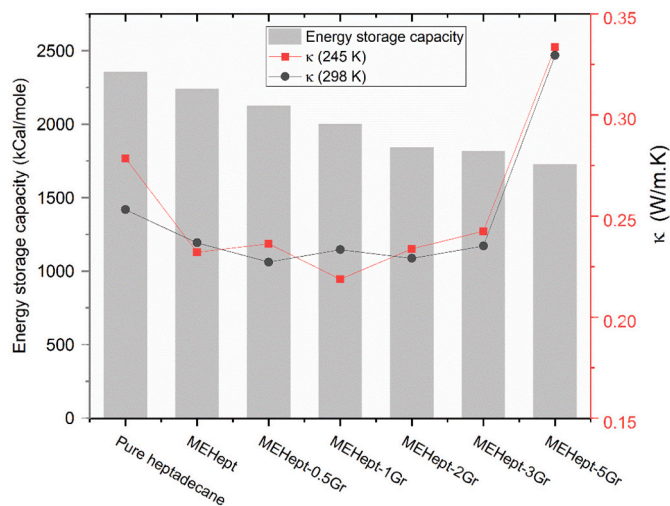
Fig. 16. Thermal conductivity of pure heptadecane and composite MEHept at 298 K.

MEHept in x, y, and z direction was respectively calculated as 0.226 W/m·K, 0.237 W/m·K, and 0.248 W/m·K, which resulted in average thermal conductivity of 0.237 W/m·K. This value shows that the PMF shell material could reduce thermal performance by about 6.49 % than that of pure n-heptadecane. The decrease in thermal performance is consistent with the RDF profile depicted in Fig. 14.

Various quantities of graphene were then utilised to examine the thermal conductivity enhancement of MEHept, and the temperature gradient of each sample is exhibited in Fig. A-6 at 245 K and 298 K. The simulated thermal conductivity of composite MEHept at 245 K and 298 K was summarised in Table 3 and visualised in Fig. 16.

As shown in Table 3 and Fig. 16, the increasing mass of graphene does not always improve thermal performance of the system, as also reported by Zhang et al. [31]. The thermal conductivity improvement of MEHept at 298 K occurred when 5 wt% of graphene was added, and achieved 39.20 % and 30.16 % enhancement more than that of MEHept and pure heptadecane at 298 K, respectively. Meanwhile, thermal conductivity improvement of MEHept at 245 K was observed for all the samples, except MEHept-1Gr. The results indicated that the thermal conductivity of MEHept was influenced by the temperature.

Analysis of the results show that the best enhancement of MEHept at 298 K occurred only when using 5 wt% of graphene. Therefore, the MEHept-5Gr with encapsulation efficiency of 73.35 % was selected for the enhanced MCM.
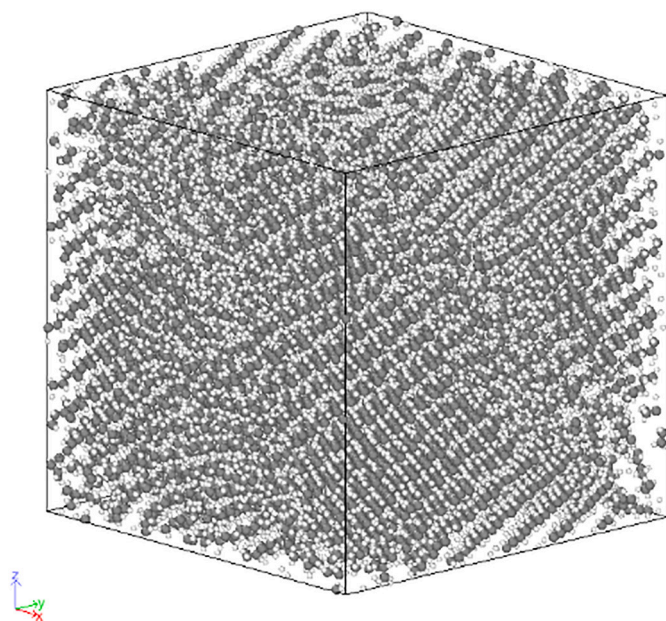
Fig. 17. Crystalline structure of octacosane.
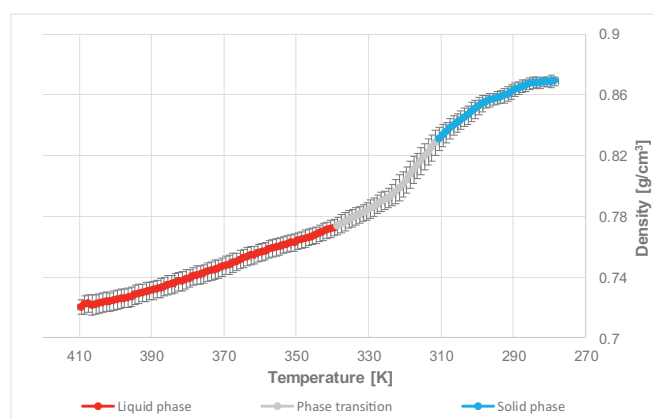
(a)
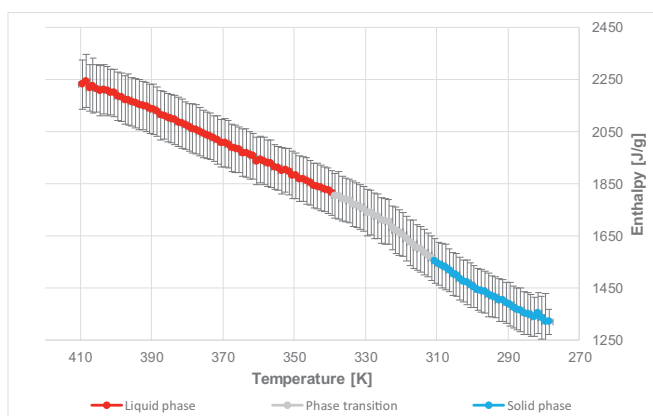
(b)

Fig. 18. The averaged (a) density and (b) enthalpy profile of pure octacosane during crystallisation.

3.2. Octacosane and microencapsulated octacosane (MEOct)

3.2.1. Pure octacosane

Similar to the heptadecane model, the octacosane was cooled down to obtain crystalline structure. After cooling process from 384 K to 284 K in NPT ensemble, octacosane crystal structure was obtained as displayed in Fig. 17.

The density profile in Fig. 18(a) was obtained throughout the cooling process. In accordance with the energy profile, it is apparent that the phase change takes place within the temperature range of 319.51 K to 345.49 K. The calculated average temperature during the phase transition is determined to be 332.50 K. The result is almost consistent as reported by Sari et al. [17] at 333.64 K. Simultaneously, the density is determined to be 0.81 g/cm^3, which corresponds to the data presented in Reference [18].

The enthalpy profile of solidified octacosane was obtained as shown in Fig. 18(b). The energy storage is estimated by measuring the enthalpy change that occurs during the phase transition. The calculated value was about 2523.01 kCal/mol, which is equivalent to 217.40 J/g. This computed latent heat is slightly less than the value reported by Sari et al. [17], which is 258.42 J/g.

Fig. 19(a) demonstrates a direct relationship between the temperature of octacosane and the development rate of MSD. The MSD curve for octacosane had a conspicuous rise in slope, demonstrating a more prominent inclination during the temperature range of 324–334 K. This is also can be seen in self-diffusion coefficient in Fig. 19(b) as the intersection of lines at about 333 K.

Fig. 20 shows the RDF profile of pure octacosane at temperatures ranging from 284 K to 384 K. With an increase in temperature, the intensity of the RDF peak lowers, indicating a decline in the order parameter of octacosane during phase transition. Furthermore, the primary peaks of octacosane are located at almost identical distances to those of heptadecane, specifically at 2.55 Å, 6.85 Å, and 9.25 Å. This indicates that the distribution of alkanes remains constant when they interact with each other [30].

For the purpose of determining thermal conductivity, a simulated box containing pure octacosane was constructed as 45.65 Å × 45.60 Å × 45.61 Å. Fig. 21(a) depicts the correlation between the simulation time and the energy of octacosane at 298 K in *x* direction. The average heat flux along the *x*, *y*, and *z* axes were 0.044 kCal/mol fs, 0.032 kCal/mol fs, and 0.027 kCal/mol fs, respectively.

The thermal conductivity of octacosane was determined in three different directions, yielding values of about 0.490 W/m·K, 0.326 W/m·K, and 0.278 W/m·K. Finally, the average thermal conductivity at 298 K was calculated as 0.365 W/m·K.

3.2.2. Microencapsulated octacosane (MEOct)

Fig. 22 exhibits the density profile of MEOct. A distinct change in slope is seen in the temperature range from 320 K to 340 K. This is potentially the region of phase transition as also demonstrated by MSD profile in Fig. 23(a). The gradient of the MSD curve increased significantly, becoming more prominent between 324 K and 334 K, indicating the phase transition region.

In addition, the intersection line is obviously seen in self-diffusion in the Fig. 23(b). Therefore, the phase transition temperature of MEOct was determined at 329.49 K.

Based on the previously indicated phase transition zone, the enthalpy can be approximated using Fig. 24. The value was found around 2099.77 kCal/mol, which is equivalent to 89.33 % of the energy storage capacity of pure octacosane.

Fig. 25 illustrates the RDF for the MEOct sample. Similar to heptadecane and MEHept, the main peak of the RDF for pure octacosane is also greater than that of MEOct. This reveals that the thermal response has been decreased, resulting in a reduction in thermal performance.

In an attempt to investigate the phase transition, the same method was also adopted for MEOct at various graphene weights. The density
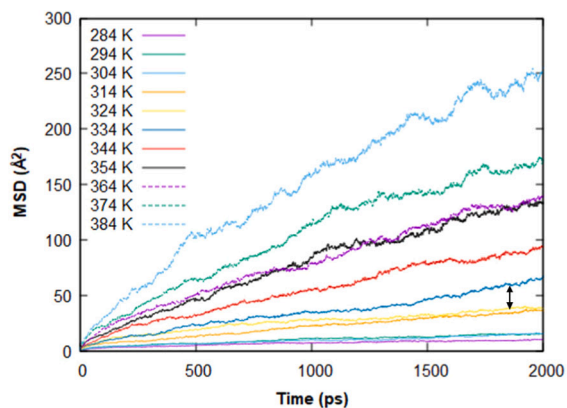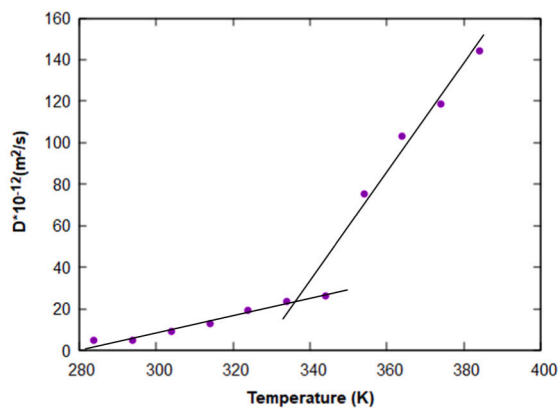
Fig. 19. The simulated (a) MSD and (b) self-diffusion coefficient of pure octacosane.
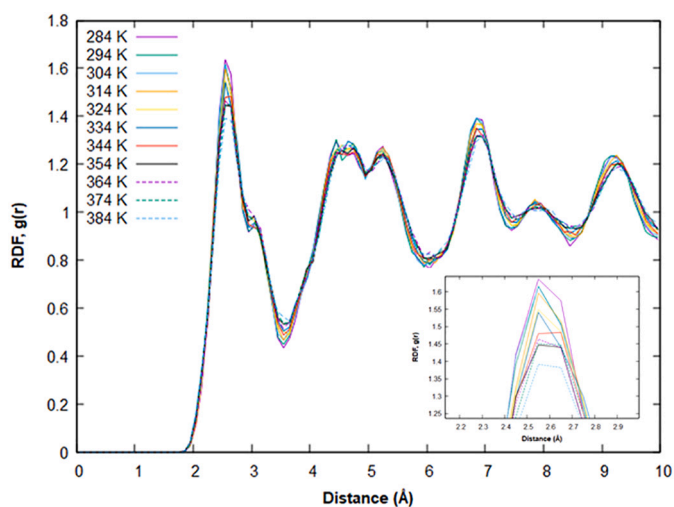
Fig. 20. The RDF of pure octacosane.

Fig. B-2 displays the computed MSD for all composite MEOct samples. It can be seen that the slopes for MEOct-1Gr, MEOct-2Gr, and MEOct-3Gr underwent a sudden change at a temperature of 284 K, indicating the onset of phase transition. On the other hand, the abrupt change in gradient for MEOct-0.5Gr and MEOct-5Gr were observed higher than 284 K. These findings confirmed the results in the density profile displayed in Fig. B-1.

The intersecting lines in the self-diffusion coefficient profile in Fig. B-

Fig. 22. The density profile of MEOct.

profile, as seen in Fig. B-1, provides indications of the phase transition in composite MEOct samples. The phase transition of most composite MEOct samples occurred in the temperature range of 320 K to 340 K. This phase transition had similarities to the phase change seen in pure octacosane and MEOct. Nevertheless, the MEOct-0.5Gr and MEOct-5Gr exhibited much higher phase transition temperatures than pure octacosane, at 377 K and 369 K, respectively.

Fig. 21. The (a) energy and (b) temperature gradient of octacosane in x direction at 298 K.
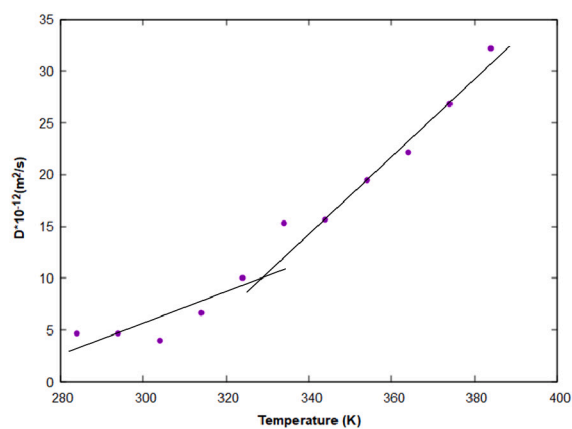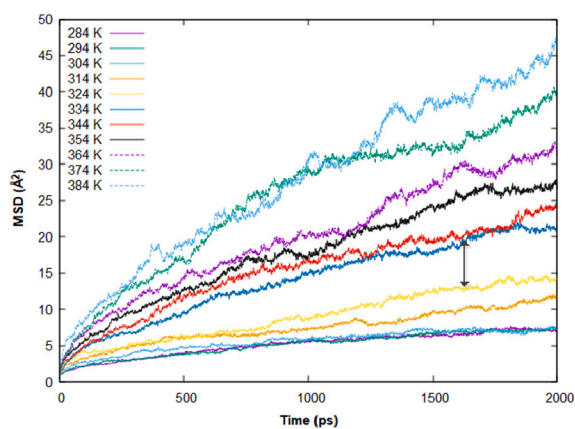
(a)

(b)

Fig. 23. The simulated (a) MSD and (b) self-diffusion coefficient of MEOct.
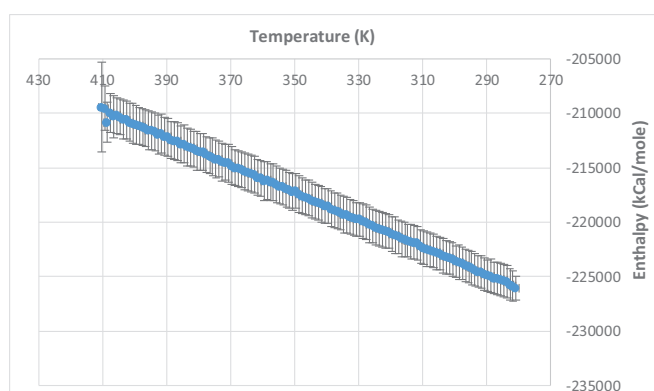
Fig. 24. The enthalpy profile of MEOct.
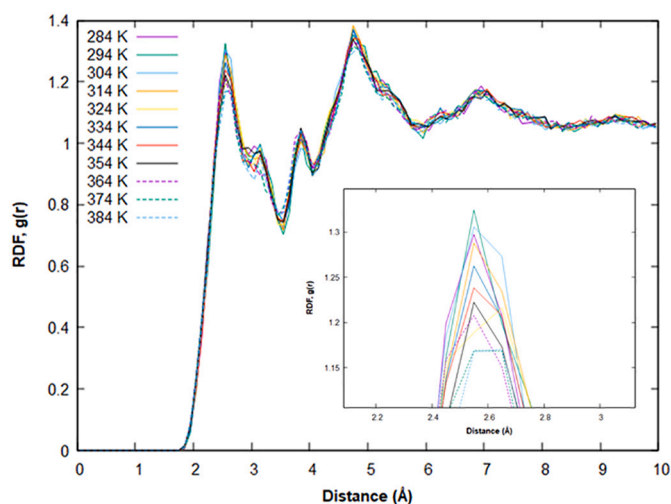
Fig. 25. The RDF of MEOct.

3 could also be used for predicting the phase transition temperature of composite MEOct samples. The phase change temperature of MEOct-1Gr, MEOct-2Gr, and MEOct-3Gr were comparable to that of pure octacosane, at 331.51 K, 330.99 K, and 330.01 K, respectively. Conversely, the phase transition temperature of MEOct-0.5Gr and MEOct-5Gr appeared 39 K - 47 K higher than that of pure octacosane.

The enthalpy of composite MEOct samples can potentially be estimated by referring to Fig. B-4. The phase transition thermophysical properties of pure octacosane and composite MEOct samples were then presented in Table 4. Like MEHept, due to the introduction of graphene, the energy storage of composite MEOct was gradually decreased. In comparison to the MEOct without graphene, the highest reduction of energy storage capacity was found about 20 % when 5 wt% of graphene was added.

Fig. B-5 displays the RDF profile of MEOct samples containing graphene concentrations ranging from 0.5 wt% to 5 wt%. The RDF results were recorded at temperature range of 284 K to 384 K. The peak value of the RDF in the solid state is visibly greater than the peak in the liquid state, owing to the more compact arrangement of atoms in the solid state. Like composite MEHept, the main peak values of composite MEOct also exhibited increases with the addition of graphene, indicating the possibility of improved thermal performance.

The thermal conductivity of MEOct was then computed at 298 K using NEMD method. The average energy for 500,000 fs, as exhibited in Fig. 26(a) for x direction, was then computed. The values were found by about 0.033 kCal/mol fs, 0.034 kCal/mol fs, 0.036 kCal/mol fs at x, y, and z direction, respectively. Meanwhile, the average temperature gradient in the x direction in Fig. 26(b) was found as 1.433 K/Å, while in y and z directions were obtained respectively as 1377 K/Å, and 1.385 K/Å. By employing the average energy and temperature gradients, the thermal conductivity was obtained by 0.241 W/m·K, 0.258 W/m·K, and 0.275 W/m·K at x, y, and z directions, and resulted in average thermal conductivity of 0.258 W/m·K. Therefore, due to the encapsulation using PMF shell material, the thermal conductivity of MEOct was 29.23 % lower than that of pure octacosane at 298 K.

As the addition of graphene at various compositions in MEOct, the thermal conductivity was also investigated and the gradient temperatures are exhibited in Fig. B-6. Next, the results were summarised in Table 4 and visualised in Fig. 27.

Table 4

Thermophysical properties of pure octacosane and MEOct samples.

Sample	Phase transition		Encapsulation Efficiency (%)	Thermal conductivity (κ) ((W/m·K)) at 298 K			
	Temperature (K)	Enthalpy (kCal/mol)		κ_x	κ_y	κ_z	κ_{ave}
Pure octacosane	330.00	2523.01	–	0.490	0.326	0.278	0.365 ± 0.111
MEOct	329.49	2099.77	83.22	0.241	0.258	0.275	0.258 ± 0.017
MEOct-0.5Gr	377.00	1907.44	75.60	0.273	0.266	0.261	0.266 ± 0.006
MEOct-1Gr	331.51	1855.75	73.55	0.293	0.268	0.227	0.263 ± 0.033
MEOct-2Gr	330.99	1784.63	70.73	0.357	0.250	0.253	0.287 ± 0.061
MEOct-3Gr	330.01	1713.17	67.90	0.403	0.340	0.198	0.314 ± 0.105
MEOct-5Gr	369.00	1679.72	66.58	0.453	0.592	0.209	0.418 ± 0.194

(a)   (b)
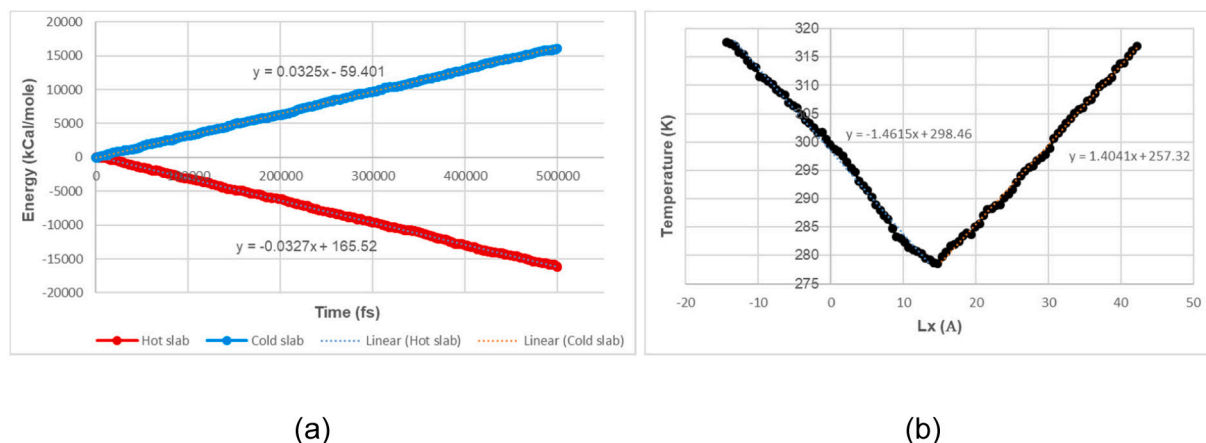
Fig. 26. The (a) energy and (b) temperature gradient of MEOct in *x* direction at 298 K.
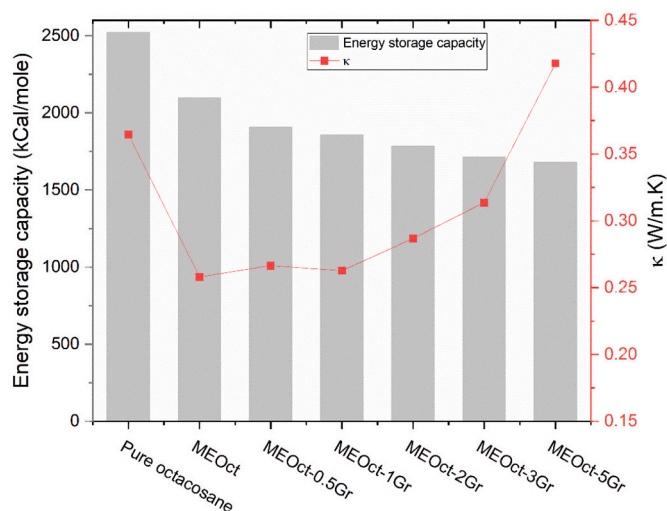
Fig. 27. Thermal conductivity of pure octacosane and composite MEOct at 298 K.

Fig. 27 exhibits the thermal conductivity of pure octacosane and MEOct samples. It was found that the thermal conductivity of composite MEOct rose gradually with the addition of graphene from 0.5 % to 5 %. The thermal performance of MEOct was improved by 1.02 until 1.62

times than the sample without graphene.

Due to the addition of 5 wt% graphene to MEOct, the thermal conductivity improvement was found by 61.95 %. However, the energy storage capacity was lowered by 25.01 % than that of MEOct-0Gr. The results demonstrated that the use of 5 wt% graphene had a more pronounced impact on enhancing thermal performance compared to reducing latent heat. Thus, the MEOct-5Gr with the encapsulation efficiency of 66.58 %, was adopted for the enhanced MCM.

3.3. Multiphase change material (MCM)

Due to the obtained results of composite MEPCMs, 5 wt% of graphene was selected for the enhancement of MCM. The density of MCMs shown in Fig. 28 exhibited varying gradients over several regions, which potentially indicates the phase transition as represented by the white lines. Fig. 28(a) shows the phase transition temperature ranges of MCM-0Gr, indicated by the distinct gradients at 287 K – 295 K and 347 K – 355 K. Meanwhile, the MCM-5Gr (Fig. 28 (b)) had phase change temperatures in the range of 288 K – 295.5 K and 341 K – 335 K. This observation indicates that the phase transition temperatures of MCM do not consistently correspond to those of each MEPCM.

The simulated MSD curves of MCM-0Gr is presented in Fig. 29(a). The linearity of the MSD system was also demonstrated over time. The observations indicate that the MSD curve exhibited a fairly flat trend up to 285 K, but then progressively increase steeper after 295 K, indicating the initial melting of MCM-0Gr. Fig. 29(b) shows the self-diffusion
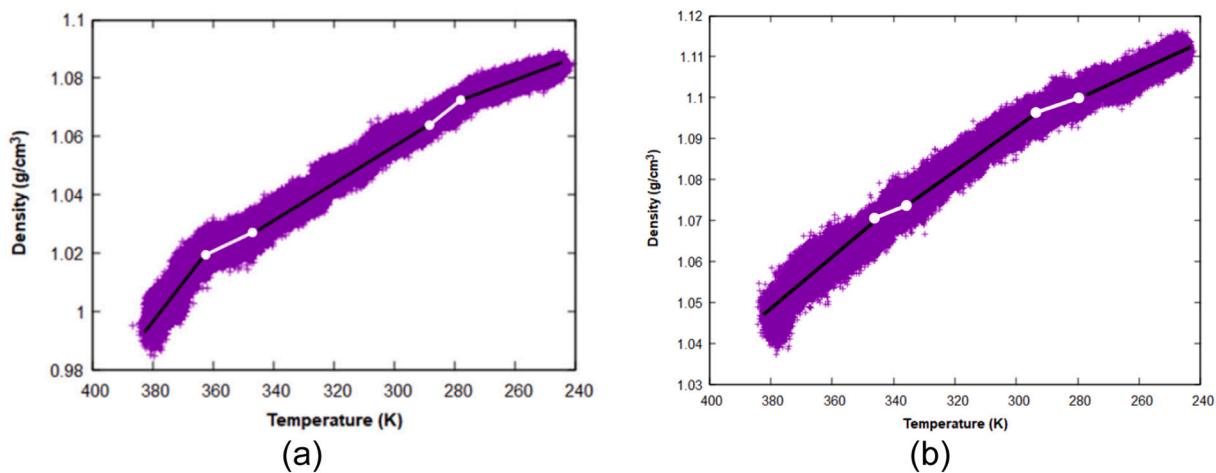
Fig. 28. The density profile of (a) MCM-0Gr and (b) MCM-5Gr.
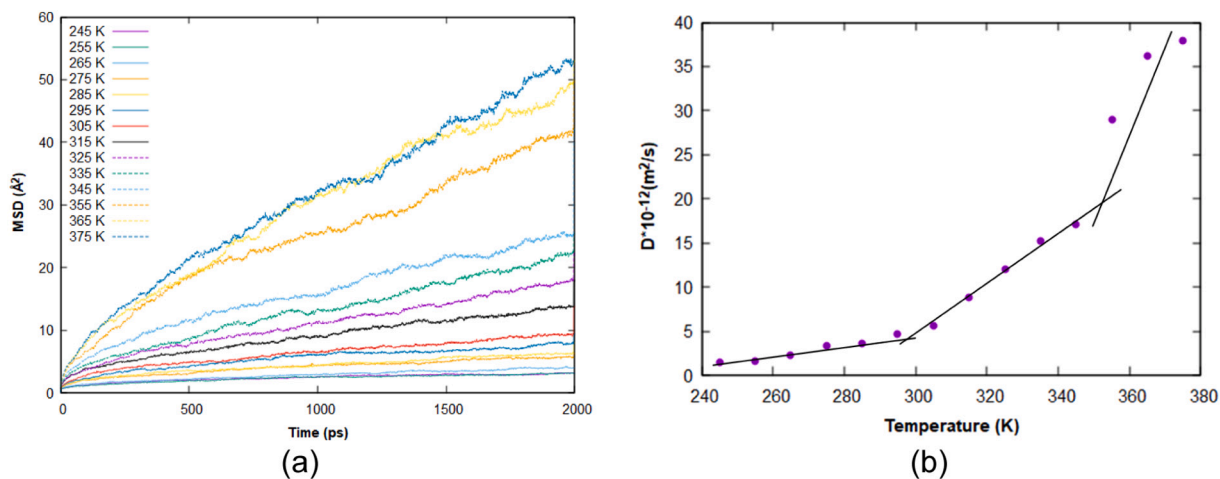
Fig. 29. The simulated (a) MSD and (b) self-diffusion coefficient of MCM-0Gr.
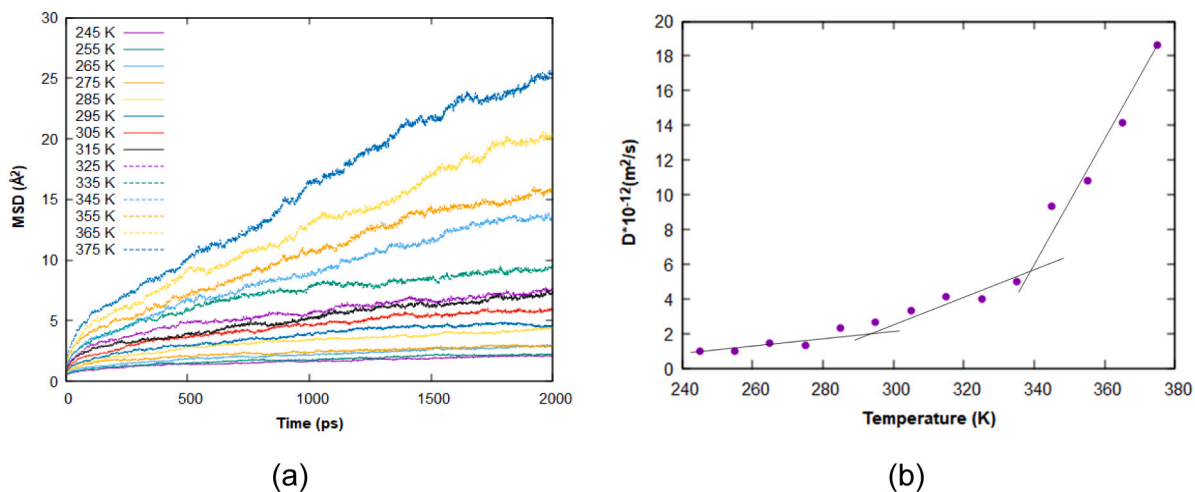
Fig. 30. The simulated (a) MSD and (b) self-diffusion coefficient of MCM-5Gr.
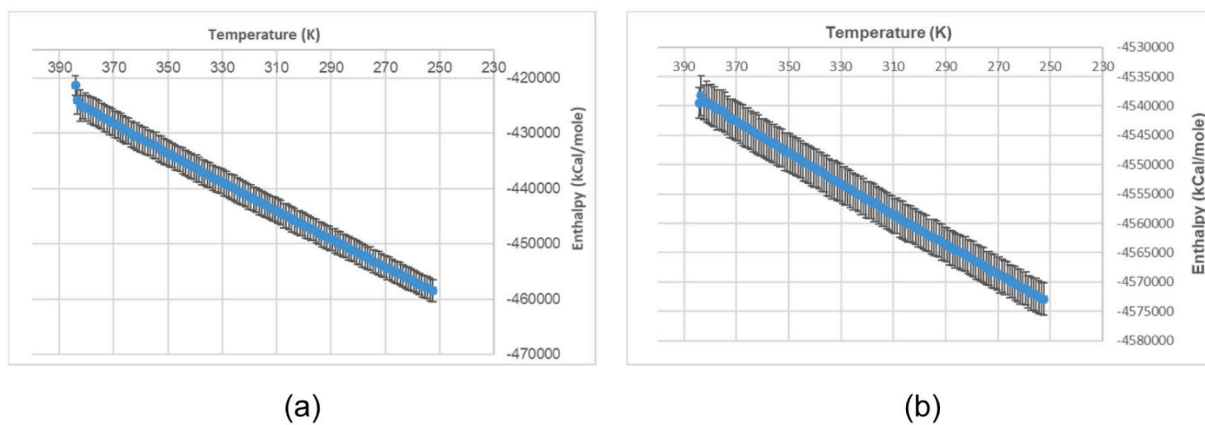
Fig. 31. The enthalpy profile of (a) MCM-0Gr and (b) MCM-5Gr.
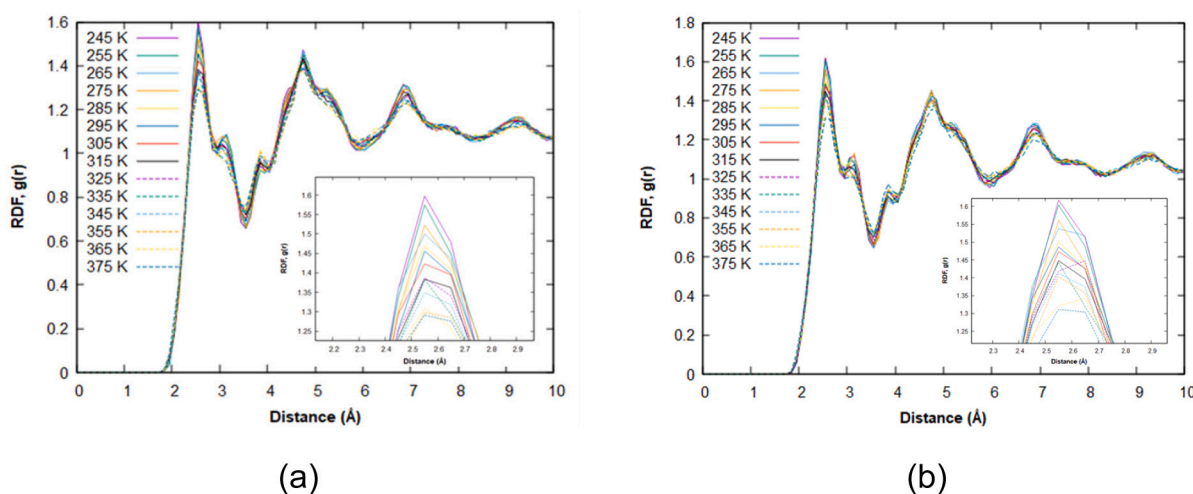
Fig. 32. The RDF of (a) MCM-0Gr and (b) MCM-5Gr.
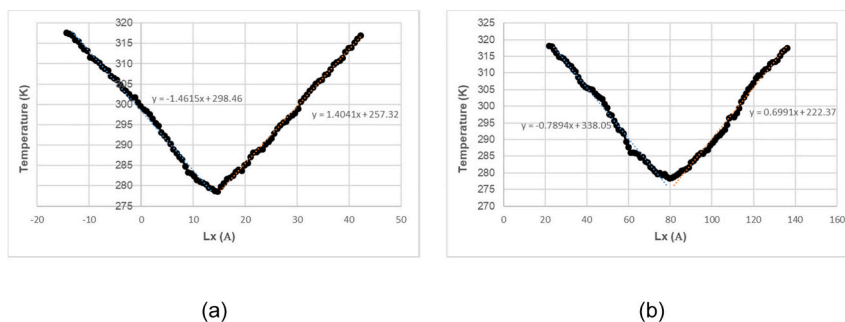
Fig. 33. Temperature gradient of (a) MCM-0Gr, and (b) MCM-5Gr for *x* direction at 298 K.

Table 5
Thermophysical properties of MCMs.

Sample	Phase transition			Encapsulation Efficiency (%)	κ_{ave} ((W/m·K)) at 298 K
	1st Temp (K)	2nd Temp (K)	Total Enthalpy (kCal/ mol)		
MCM-0Gr	291.51	351.51	4387.85	89.99	0.211 ± 0.076
MCM-5Gr	292.00	338.48	3454.27	70.84	0.282 ± 0.107

coefficient of MCM-0Gr. It can be seen clearly the multiple points were obtained as the intersection of linear regression over all data points, which is located at about 292 K and 352 K. These findings were consistent with the density profile depicted in Fig. 28.

The MSD and self-diffusion coefficient of MCM-5Gr are depicted in Fig. 30, respectively. Fig. 30(a) demonstrates how MSD changed in the MCM-5Gr at different temperatures. The MSD of MCM-5Gr exhibited a more flat gradient as compared to the MCM-0Gr, which might be attributed to the presence of graphene inside the MCM. According to the self-diffusion coefficient in Fig. 30(b), MCM-5Gr had multiple points at about 292 K and 338.48 K, which refers to the phase transition

temperature of heptadecane and octacosane, respectively.

The enthalpy profiles in Fig. 31 were subsequently employed to estimate the energy storage capacity of MCM in each temperature region. The latent heat values of MCM-0Gr were determined totally to be around 4387.85 kCal/mol at temperature range of 287–295 K and 347–355 K. Meanwhile, the MCM-5Gr had total energy storage capacity of 3454.27 kCal/mol at temperature range of 288.5–295.5 K and 335.5–341.5 K.

In comparison with the MEPCMs, the overall energy storage capacity of MCMs is about 1.13 %–1.40 % higher than total latent heat of MEHept and MEOct. The disparity in latent heat between those values was below 5 %, indicating that the results were reliable.

The calculated RDF of MCM-0Gr and MCM-5Gr are presented respectively in Fig. 32(a) and Fig. 32(b). The main peaks were seen at distance of 2.55 Å, 4.75 Å, 6.55 Å, and 9.25 Å. Furthermore, the intensity of the peaks weakened as the temperature rose within the range of 245 K to 375 K, as shown in the magnified picture of the peaks. Furthermore, it could be noticed that the decline or weakening of the primary peaks in the MCMs is smaller when compared to pure heptadecane and octacosane. This confirms a substantial reduction in the thermal performance of MCMs. However, in comparison to MCM-0Gr, the MCM-5Gr exhibited a rising pattern of main peaks, indicating the improved thermal conductivity.

To be able to compute thermal conductivity of MCM, the structure model was constructed in a simulation box with a dimension of 114.61 Å $\times$ 56.45 Å $\times$ 57.41 Å.

The average energy of MCM-0Gr at each direction was then obtained by about 0.017 kCal/mol fs, 0.071 kCal/mol fs, and 0.061 kCal/mol fs. By adopting the same method, the average energy for MCM-5Gr was calculated by about 0.0173 kCal/mol fs, 0.1114 kCal/mol fs, and 0.0542 kCal/mol fs at x, y, and z axes.

Subsequently, the temperature gradient of MCM-0Gr in x axes depicted in Fig. 33(a) was computed, yielding mean values of 1.404 K/Å, while in y and z axes were respectively by 1.387 K/Å, and 1.385 K/Å. The thermal conductivities were subsequently determined and gave values of 0.125 W/m·K, 0.272 W/m·K, and 0.235 W/m·K in the x, y, and z directions accordingly. Finally, the aforementioned values were computed as the mean, resulting in a thermal conductivity of 0.211 W/m·K at a temperature of 298 K. The thermal conductivity of composite MCM at 5 wt% of graphene was also computed at 298 K, which resulted in average thermal conductivity of 0.282 W/m K.

The thermopysical properties of MCM samples were summarised and shown in Table 5. The thermal conductivity of MCM was enhanced from 0.211 W/m·K to 0.282 W/m·K by the addition of 5 % graphene, resulting in 33.75 % improvement. However, it was found 21.28 % reduction of heat storage capacity. The findings indicated that including 5 wt% graphene into MCM had a more significant effect on improving thermal performance in comparison to decreasing latent heat.

4. Conclusions

This study was focused on the theoretical investigation of an enhanced multiphase change material (MCM), which was developed by combining microencapsulated heptadecane (MEHept), microencapsulated octacosane (MEOct), and graphene additive.

The results showed that graphene was able to increase the thermal conductivity of the samples but the encapsulation efficiencies were reduced. The specific findings of study may therefore be summarised as follows:

a. The theoretical analysis found 5 wt% graphene to be the optimum amount for thermal conductivity improvement of the MEHept and MEOct by about 39 % and 62 %, compared to the sample without graphene, respectively, which therefore as the basis for the development of an enhanced MCM.

b. The MD findings also indicated that the phase transition temperatures of MCM and MEPCMs were inconsistent. It was demonstrated that MCM-0Gr exhibited multiple phase transition temperatures at 291.5 K and 351 K, whereas whereas MCM-5Gr exhibited them at 292 K and 338.5 K.

c. In comparison to the MCM-0Gr, the thermal conductivity of the MCM-5Gr was enhanced by 33.75 %, but the energy storage capacity was reduced by 21.28 %.

Even though the study has shown the potential of utilising graphene for thermal enhancement of MCM, further optimisation and validation exercises are considered to be necessary for the alignment of the results with the simulation findings.

CRediT authorship contribution statement

Rizal Sinaga: Writing – review & editing, Writing – original draft, Software, Project administration, Methodology, Investigation, Formal analysis, Data curation, Conceptualization. **Jo Darkwa:** Writing – review & editing, Writing – original draft, Supervision, Project administration, Conceptualization. **Siddig Omer:** Writing – review & editing, Supervision. **Mark Worall:** Writing – review & editing, Supervision, Conceptualization.

Declaration of competing interest

The authors declare that they have no known competing financial interests or personal relationships that could have appeared to influence the work reported in this paper.

Acknowledgement

Appendix A. Thermophysical profile of composite MEHept

(a)

(b)

(c)

(d)

(e)
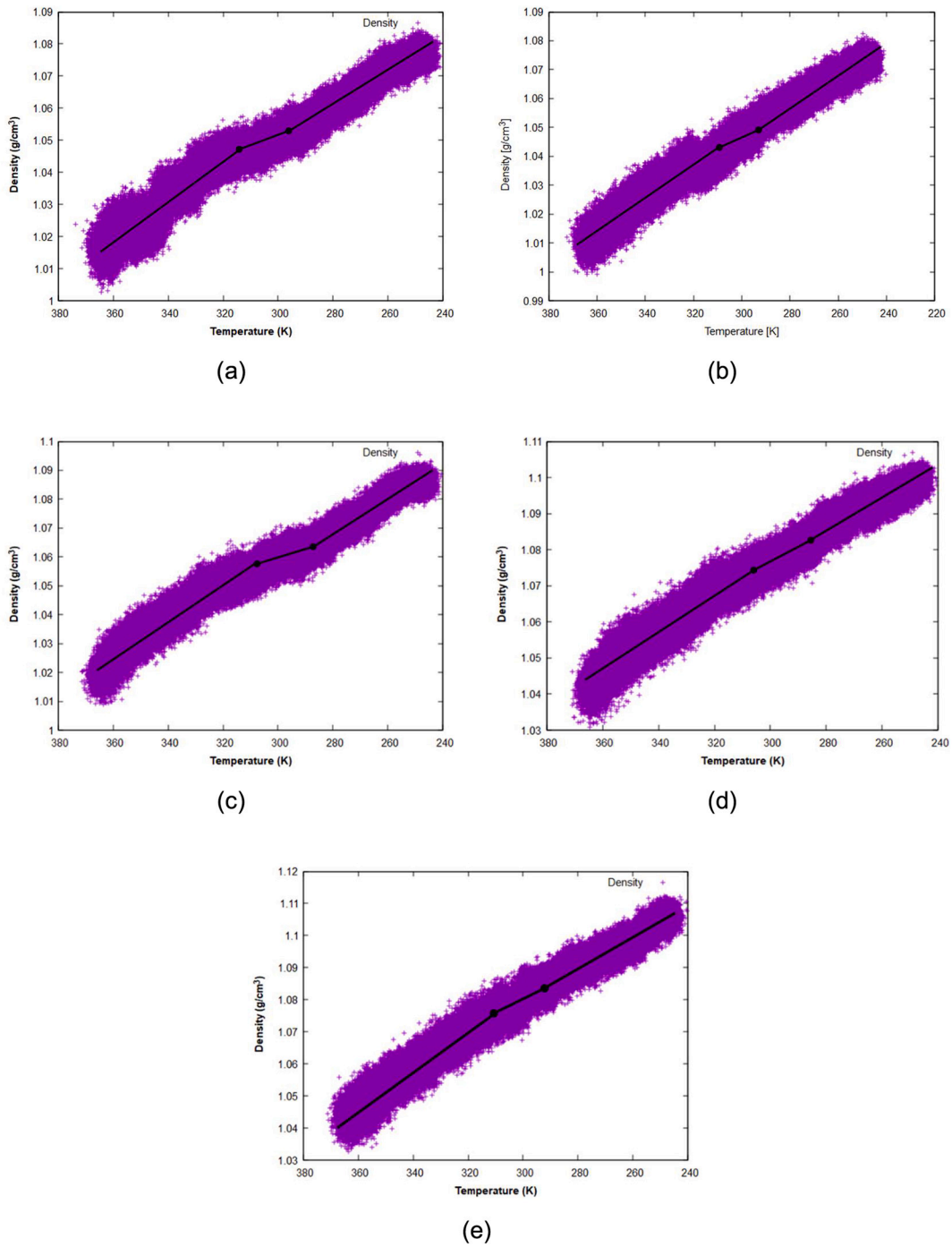
Fig. A-1. The density profile of (a) MEHept-0.5Gr, (b) MEHept-1Gr, (c) MEHept-2Gr, (d) MEHept-3Gr, and (e) MEHept-5Gr.
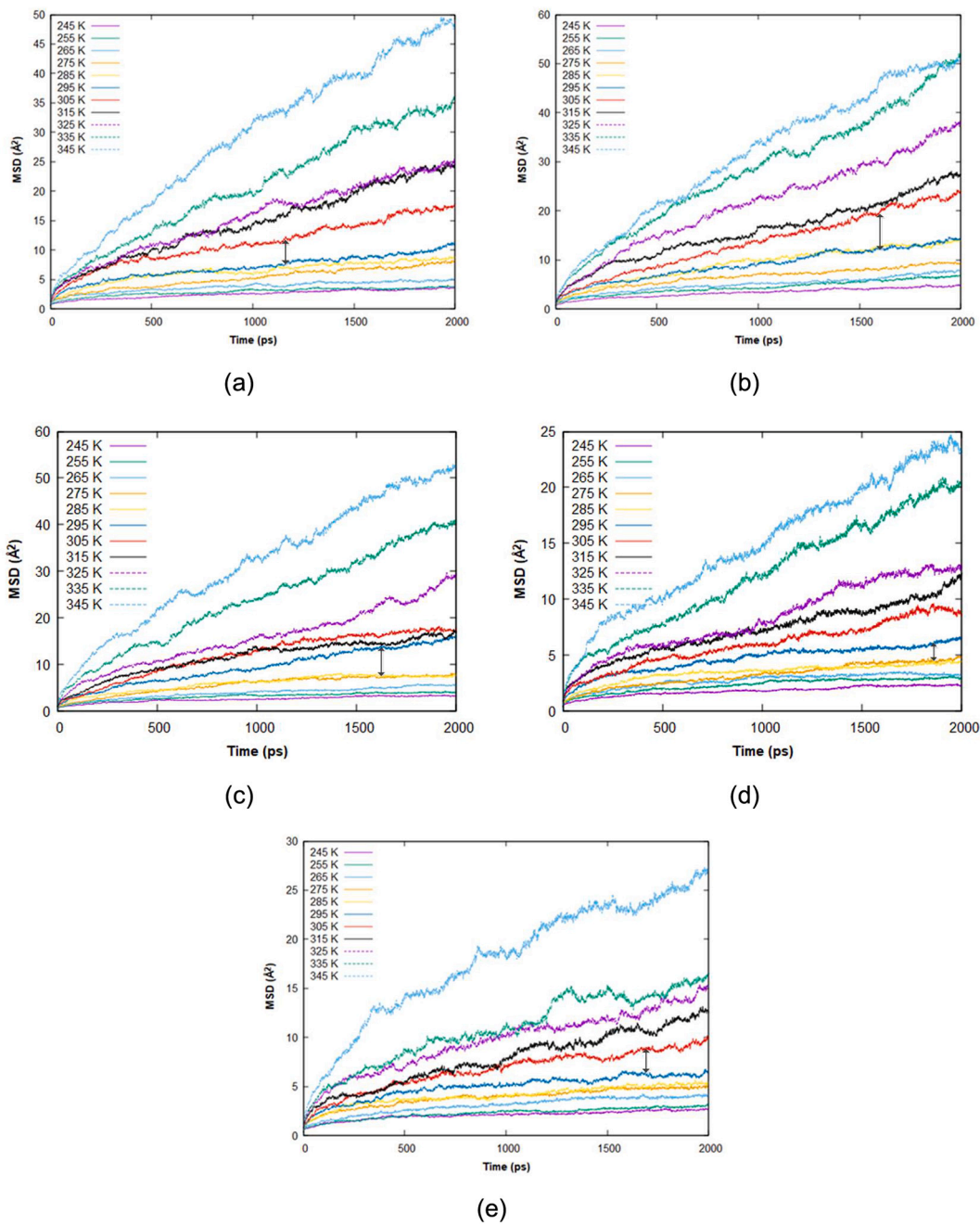
Fig. A-2. The simulated MDS of (a) MEHept-0.5Gr, (b) MEHept-1Gr, (c) MEHept-2Gr, (d) MEHept-3Gr, and (e) MEHept-5Gr.
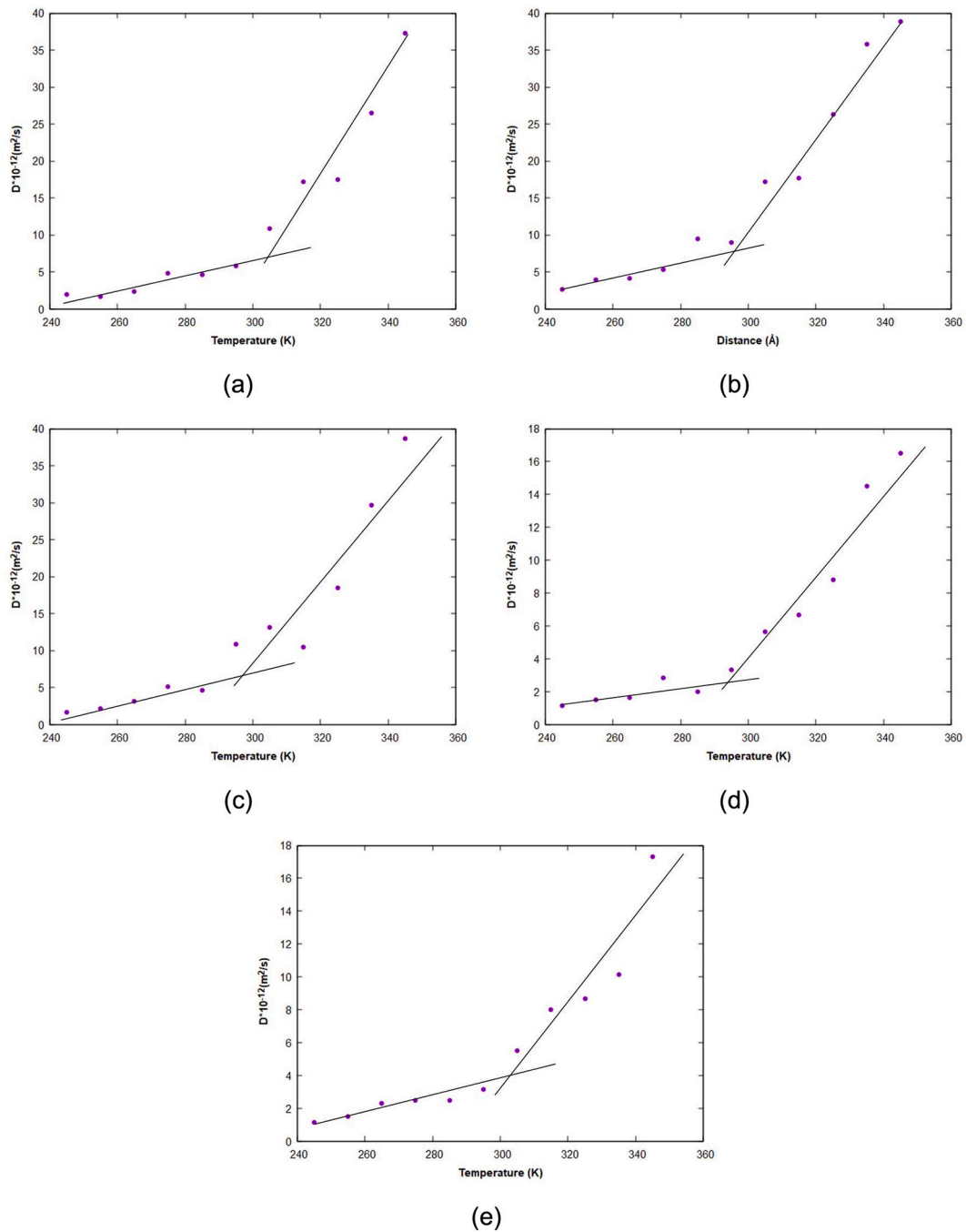
Fig. A-3. Self-diffusion coefficient of of (a) MEHept-0.5Gr, (b) MEHept-1Gr, (c) MEHept-2Gr, (d) MEHept-3Gr, and (e) MEHept-5Gr.

(a)

(b)

(c)

(d)

(e)
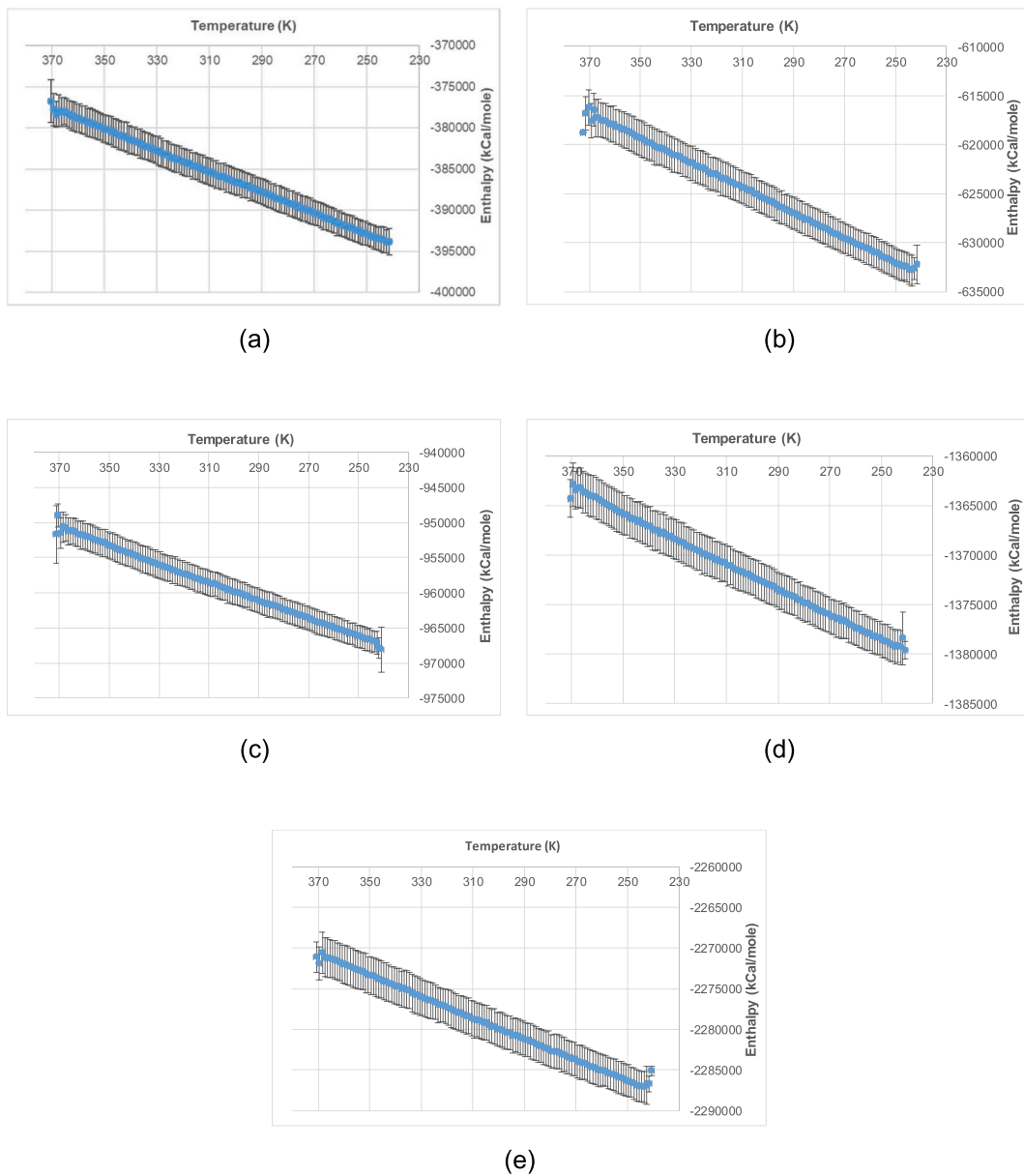
Fig. A-4. The enthalpy profile of (a) MEHept-0.5Gr, (b) MEHept-1Gr, (c) MEHept-2Gr, (d) MEHept-3Gr, and (e) MEHept-5Gr.

(a)

(b)

(c)

(d)

(e)
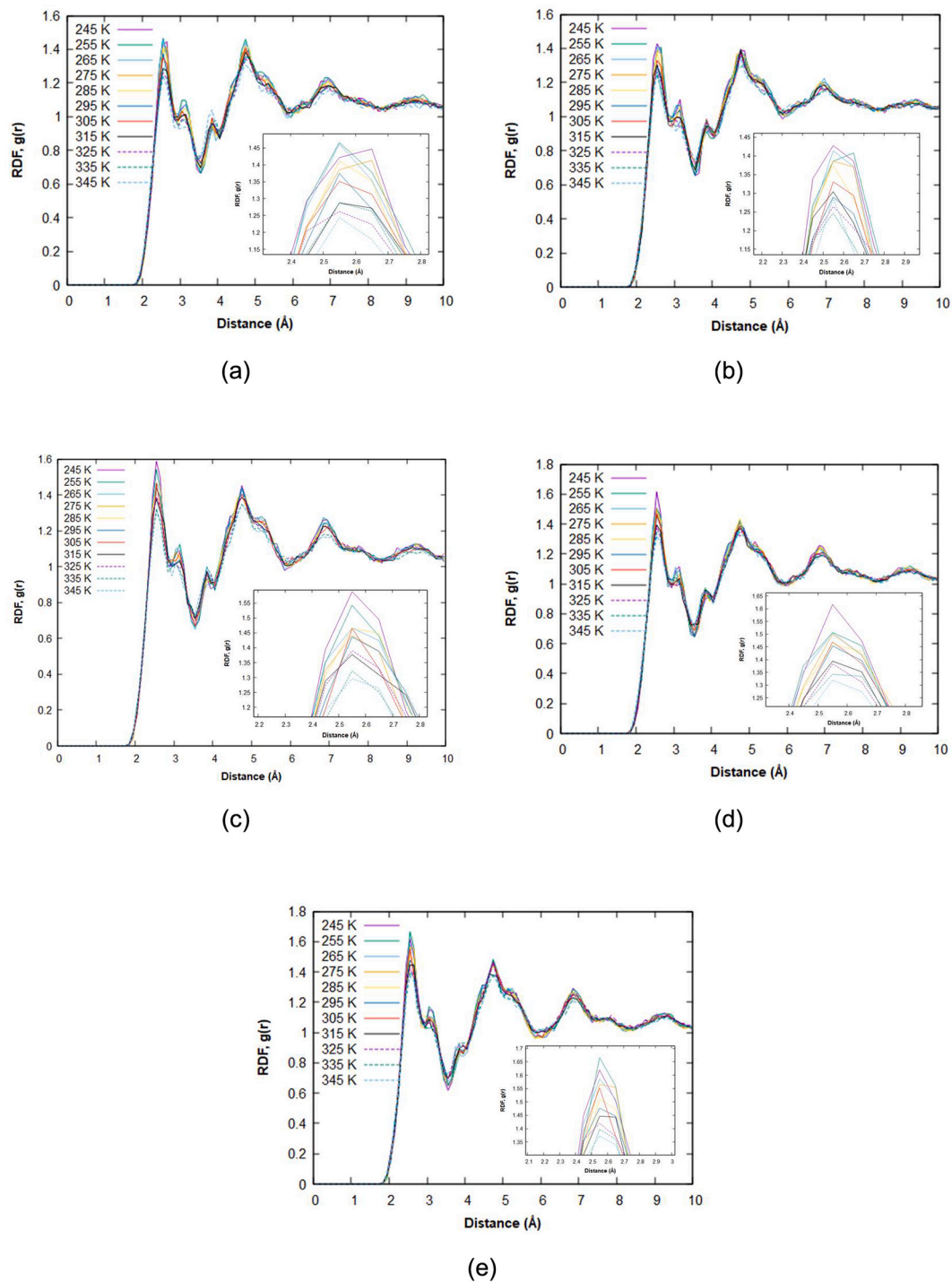
Fig. A-5. The RDF of (a) MEHept-0.5Gr, (b) MEHept-1Gr, (c) MEHept-2Gr, (d) MEHept-3Gr, and (e) MEHept-5Gr.
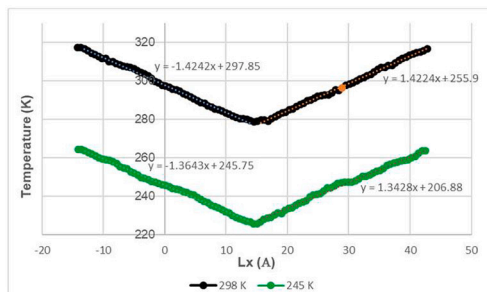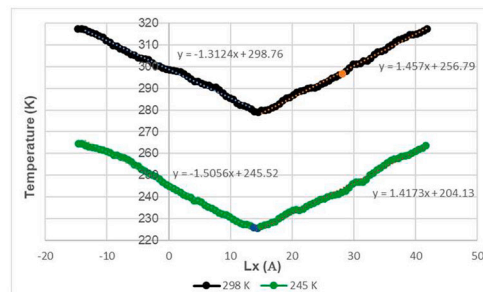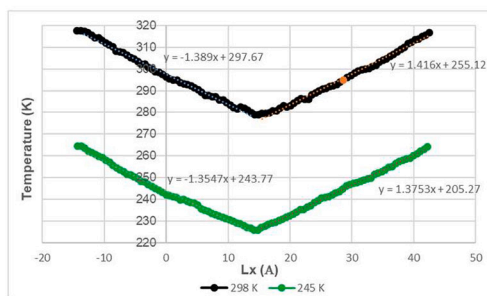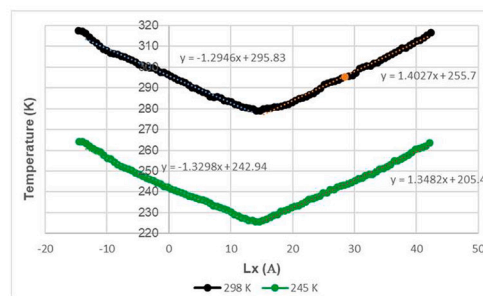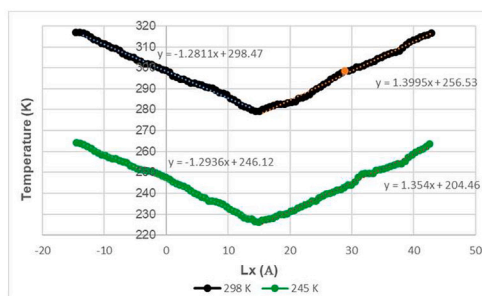
Fig. A-6. Temperature gradient of (a) MEHept-0.5Gr, (b) MEHept-1Gr, (c) MEHept-2Gr, (d) MEHept-3Gr, and (e) MEHept-5Gr in *x* direction at 245 K and 298 K.

Appendix B. Thermophysical profile of composite MEOct
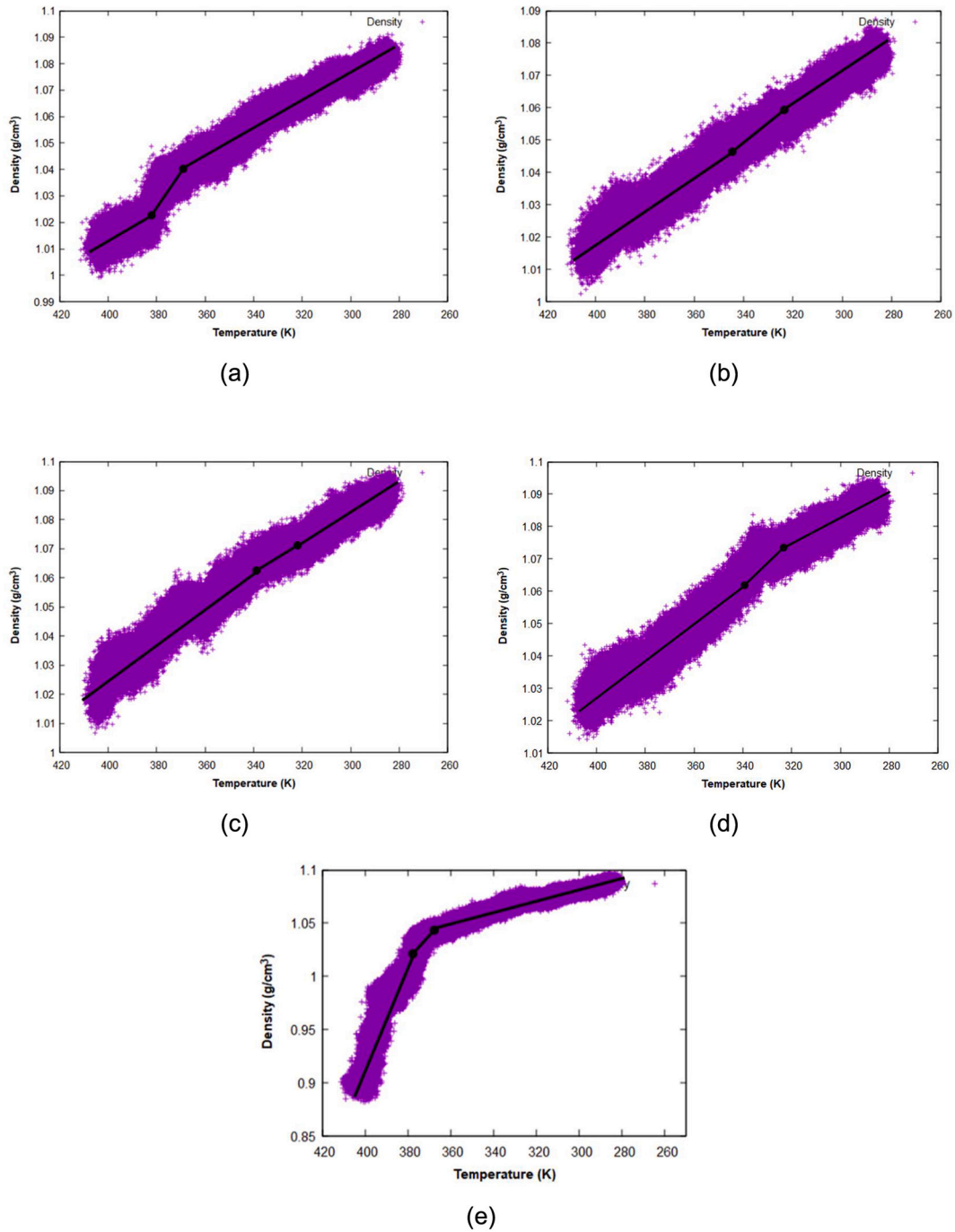
Fig. B-1. The density profile of (a) MEOct-0.5Gr, (b) MEOct-1Gr, (c) MEOct-2Gr, (d) MEOct -3Gr, and (e) MEOct-5Gr.
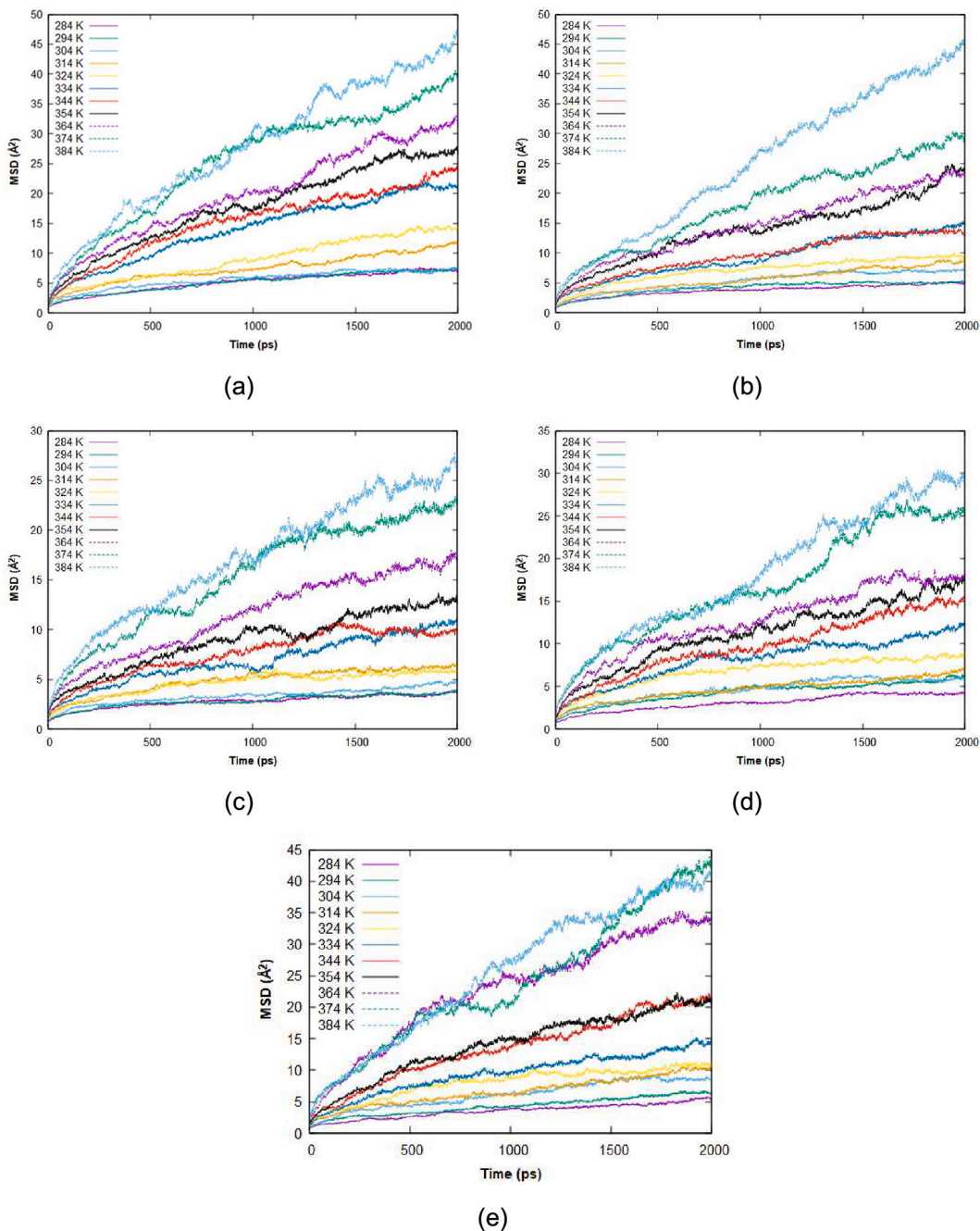
Fig. B-2. The simulated MSD of (a) MEOct-0.5Gr, (b) MEOct-1Gr, (c) MEOct-2Gr, (d) MEOct-3Gr, and (e) MEOct-5Gr.

(a)

(b)

(c)

(d)

(e)
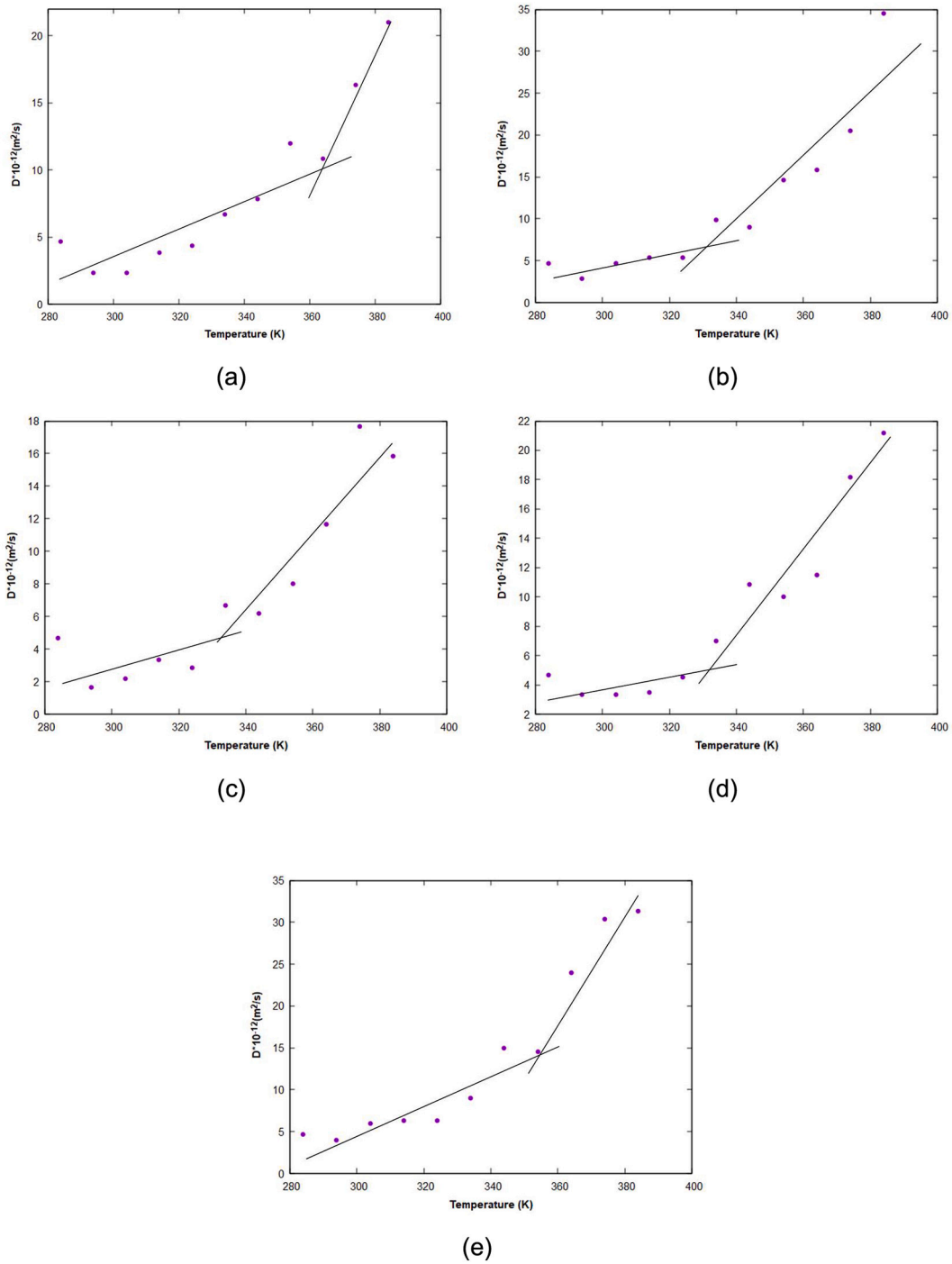
Fig. B-3. The self-diffusion coefficient of (a) MEOct-0.5Gr, (b) MEOct-1Gr, (c) MEOct-2Gr, (d) MEOct-3Gr, and (e) MEOct-5Gr.

(a)

(b)

(c)

(d)

(e)
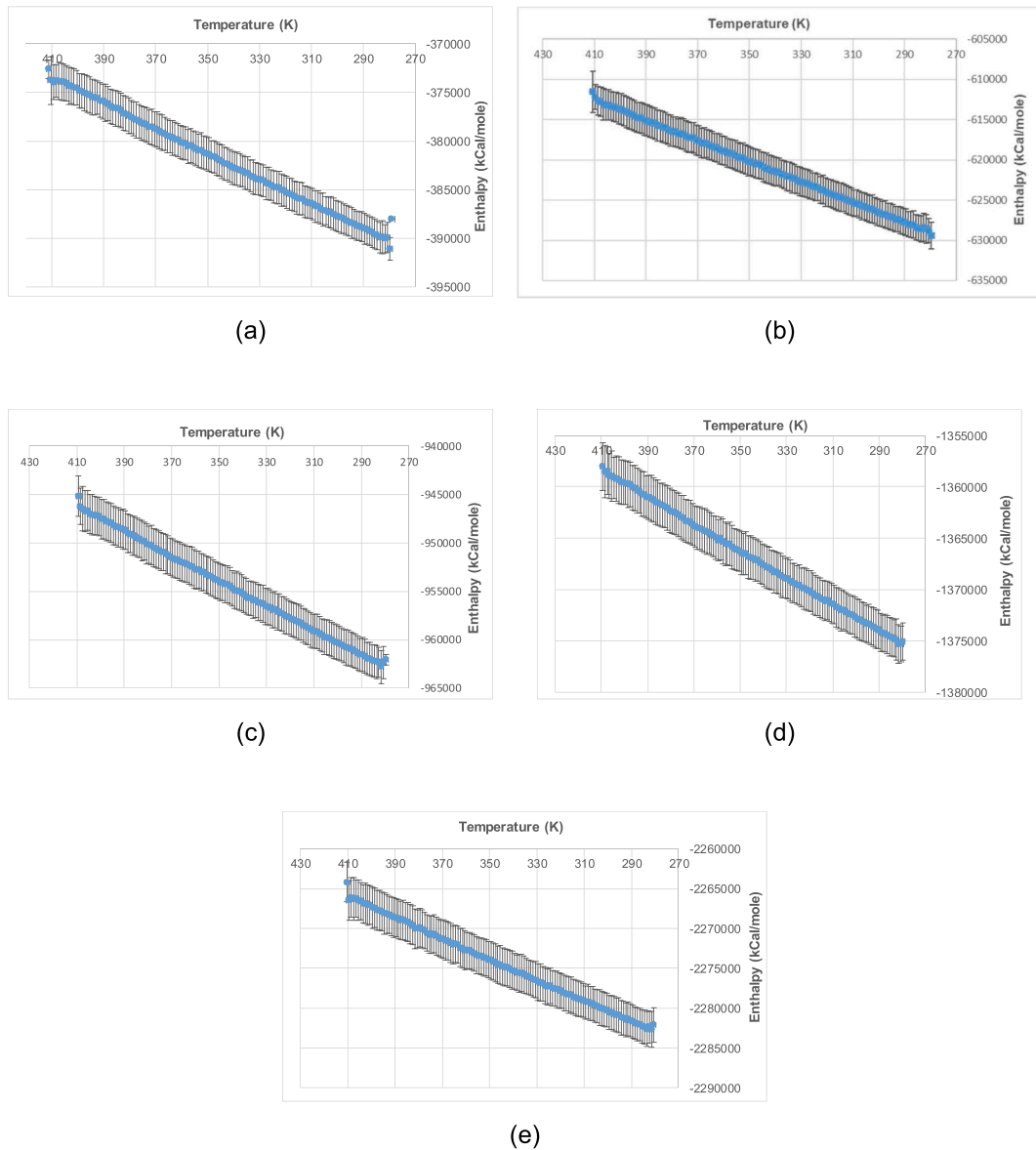
Fig. B-4. The enthalpy profile of (a) MEOct-0.5Gr, (b) MEOct-1Gr, (c) MEOct-2Gr, (d) MEOct-3Gr, and (e) MEOct-5Gr.

(a)

(b)

(c)

(d)

(e)
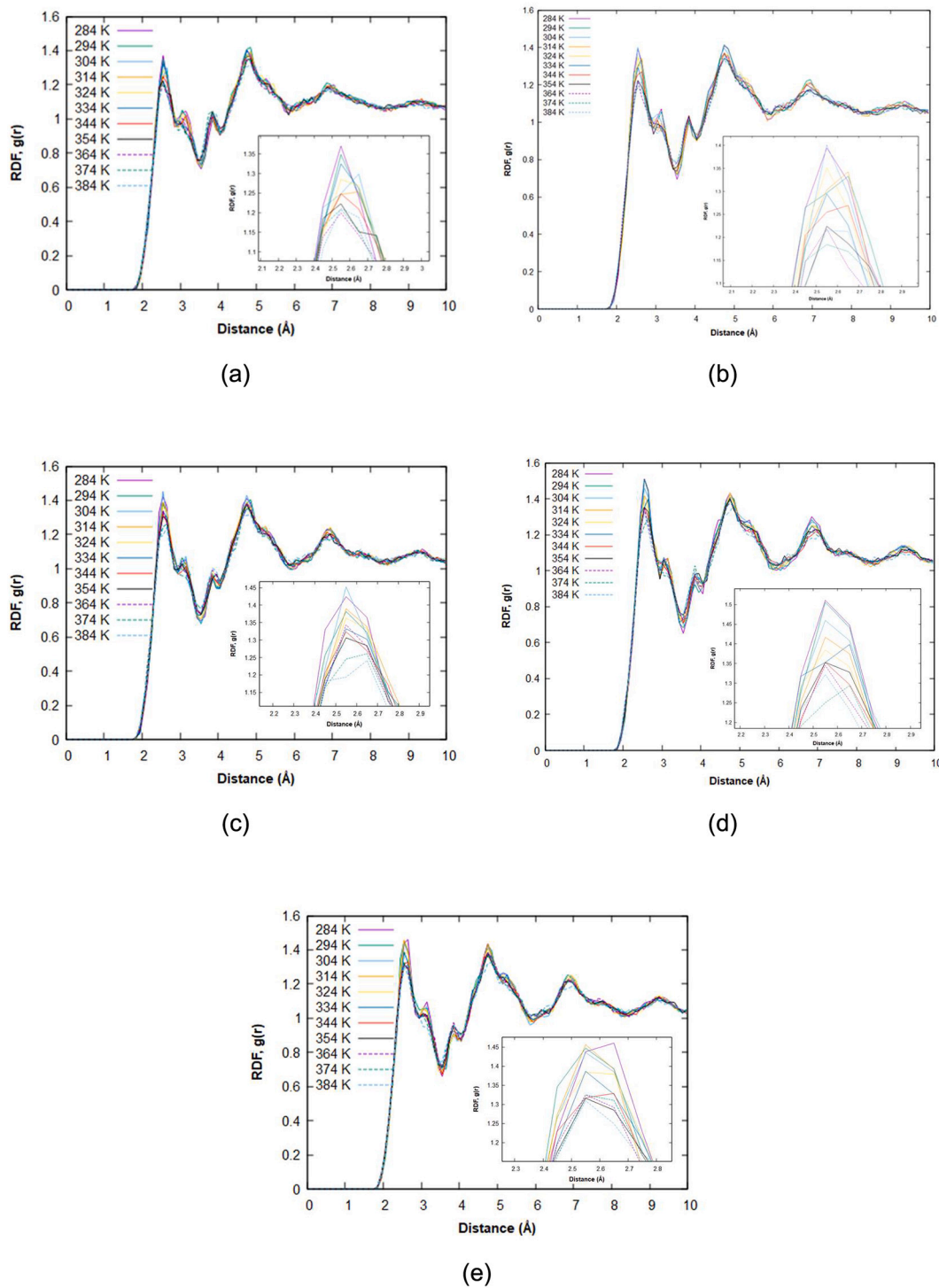
Fig. B-5. The RDF of (a) MEOct-0.5Gr, (b) MEOct-1Gr, (c) MEOct-2Gr, (d) MEOct -3Gr, and (e) MEOct-5Gr.

(a)

(b)

(c)

(d)

(e)
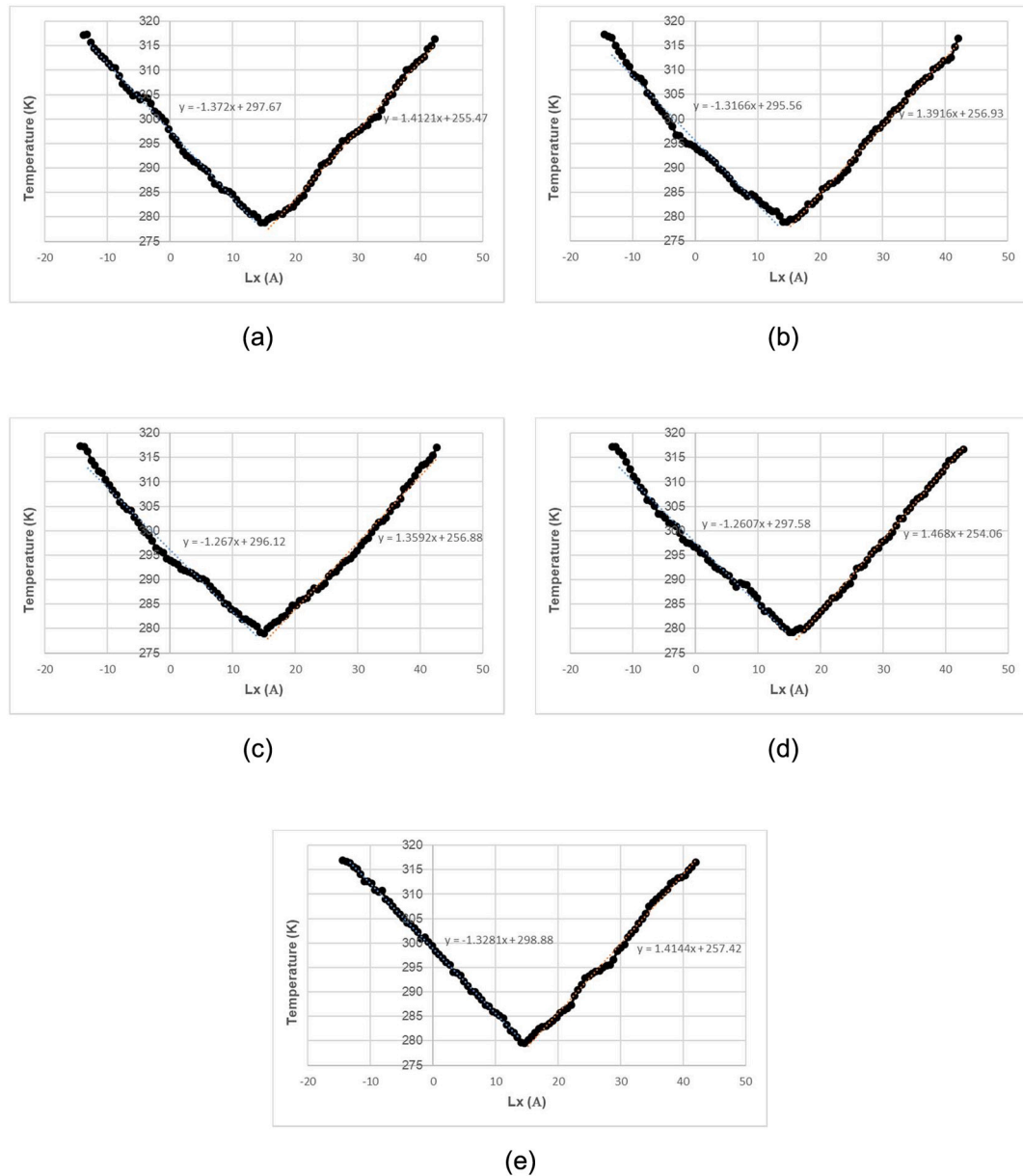
Fig. B-6. Temperature gradient of (a) MEOct-0.5Gr, (b) MEOct-1Gr, (c) MEOct-2Gr, (d) MEOct-3Gr, and (e) MEOct-5Gr in *x* direction at 298 K.

Data availability

Data will be made available on request.

References

[1] M.M. Bhatti, K. Vafai, S.I. Abdelsalam, The role of nanofluids in renewable energy engineering, Nanomaterials 13 (2023) 2–5, https://doi.org/10.3390/nano13192671.

[2] H. Zhang, Q. Dong, J. Lu, Y. Tang, W. Bi, Y. Gao, et al., Modified sodium acetate trihydrate/expanded perlite composite phase change material encapsulated by epoxy resin for radiant floor heating, J. Energy Storage 65 (2023) 107374, https://doi.org/10.1016/j.est.2023.107374.

[3] Y. Konuklu, M. Ostry, H.O. Paksoy, P. Charvat, Review on using microencapsulated phase change materials (PCM) in building applications, Energ. Buildings 106 (2015) 134–155, https://doi.org/10.1016/j.enbuild.2015.07.019.

[4] T.A. Mukram, J. Daniel, A review of novel methods and current developments of phase change materials in the building walls for cooling applications, Sustain. Energy Technol. Assess. 49 (2022) 101709, https://doi.org/10.1016/j.seta.2021.101709.

[5] N. Soares, T. Matias, L. Durães, P.N. Simões, J.J. Costa, Thermophysical characterization of paraffin-based PCMs for low temperature thermal energy storage applications for buildings, Energy (2023) 269, https://doi.org/10.1016/j.energy.2023.126745.

[6] J. Darkwa, T. Zhou, Enhanced laminated composite phase change material for energy storage, Energ. Conver. Manage. 52 (2011) 810–815, https://doi.org/10.1016/j.enconman.2010.08.006.

[7] T. Zhou, J. Darkwa, G. Kokogiannakis, Thermal evaluation of laminated composite phase change material gypsum board under dynamic conditions, Renew. Energy 78 (2015) 448–456, https://doi.org/10.1016/j.renene.2015.01.025.

[8] R.A. Kishore, M.V.A. Bianchi, C. Booten, J. Vidal, R. Jackson, Enhancing building energy performance by effectively using phase change material and dynamic insulation in walls, Appl. Energy 283 (2021) 116306, https://doi.org/10.1016/j.apenergy.2020.116306.

[9] C. Zeng, C. Yuan, H. Cao, K. Panchabikesan, F. Haghighat, Stability and durability of microencapsulated phase change materials (MePCMs) in building applications: a state of the review, J. Energy Storage 80 (2024) 110249, https://doi.org/10.1016/j.est.2023.110249.

[10] P.K. Singh Rathore, S.K. Shukla, N.K. Gupta, Potential of microencapsulated PCM for energy savings in buildings: a critical review, Sustain. Cities Soc. 53 (2020) 101884, https://doi.org/10.1016/j.scs.2019.101884.

[11] V.V. Tyagi, S.C. Kaushik, S.K. Tyagi, T. Akiyama, Development of phase change materials based microencapsulated technology for buildings: a review, Renew. Sustain. Energy Rev. 15 (2011) 1373–1391, https://doi.org/10.1016/j.rser.2010.10.006.

[12] K. Du, J. Calautit, Z. Wang, Y. Wu, H. Liu, A review of the applications of phase change materials in cooling, heating and power generation in different temperature ranges, Appl. Energy 220 (2018) 242–273, https://doi.org/10.1016/j.apenergy.2018.03.005.

[13] F. Irani, Z. Ranjbar, A. Jannesari, S. Moradian, Fabrication and characterization of microencapsulated n-heptadecane with graphene/starch composite shell for thermal energy storage, Prog. Org. Coatings 131 (2019) 203–210, https://doi.org/10.1016/j.porgcoat.2019.02.034.

[14] A. Sari, C. Alkan, D. Kahraman Döğüşcü, A. Biçer, Micro/nano-encapsulated n-heptadecane with polystyrene shell for latent heat thermal energy storage, Sol. Energy Mater. Sol. Cells 126 (2014) 42–50, https://doi.org/10.1016/j.solmat.2014.03.023.

[15] A. Sari, C. Alkan, C. Bilgin, Micro/nano encapsulation of some paraffin eutectic mixtures with poly(methyl methacrylate) shell: preparation, characterization and latent heat thermal energy storage properties, Appl. Energy 136 (2014) 217–227, https://doi.org/10.1016/j.apenergy.2014.09.047.

[16] A. Sari, C. Alkan, A. Karaipekli, O. Uzun, Microencapsulated n-octacosane as phase change material for thermal energy storage, Sol. Energy 83 (2009) 1757–1763, https://doi.org/10.1016/j.solener.2009.05.008.

[17] A. Sarı, C. Alkan, A. Biçer, Thermal energy storage characteristics of micro-nanoencapsulated heneicosane and octacosane with poly(methylmethacrylate) shell, J. Microencapsul. 33 (2016) 221–228, https://doi.org/10.3109/02652048.2016.1144820.

[18] W. Su, J. Darkwa, G. Kokogiannakis, Review of solid-liquid phase change materials and their encapsulation technologies, Renew. Sustain. Energy Rev. 48 (2015) 373–391, https://doi.org/10.1016/j.rser.2015.04.044.

[19] Y. Zhao, P. Zhang, Y. Qiu, Q. Li, H. Yan, Z. Wang, et al., Highly conductive solid-solid phase change composites and devices enhanced by aligned graphite networks for solar/electro-thermal energy storage, DeCarbon 5 (2024) 100051, https://doi.org/10.1016/j.decarb.2024.100051.

[20] R. Sinaga, J. Darkwa, M. Worall, W. Su, The effect of nucleating agent on the multiphase change materials for energy storage in buildings, Appl. Therm. Eng. 239 (2024) 122153, https://doi.org/10.1016/j.applthermaleng.2023.122153.

[21] Y. Ma, X. Chu, W. Li, G. Tang, Preparation and characterization of poly(methyl methacrylate-co-divinylbenzene) microcapsules containing phase change temperature adjustable binary core materials, Sol. Energy 86 (2012) 2056–2066, https://doi.org/10.1016/j.solener.2012.04.008.

[22] Y. Ma, S. Sun, J. Li, G. Tang, Preparation and thermal reliabilities of microencapsulated phase change materials with binary cores and acrylate-based polymer shells, Thermochim. Acta 588 (2014) 38–46, https://doi.org/10.1016/j.tca.2014.04.023.

[23] Y. Ma, Q. Xie, X. Wang, Investigations on thermal properties of microencapsulated phase-change materials with different acrylate-based copolymer shells as thermal insulation materials, J. Appl. Polym. Sci. 136 (2019) 1–12, https://doi.org/10.1002/app.47777.

[24] W. Su, J. Darkwa, G. Kokogiannakis, Numerical thermal evaluation of laminated binary microencapsulated phase change material drywall systems, Build. Simul. 13 (2020) 89–98, https://doi.org/10.1007/s12273-019-0563-z.

[25] R. Sinaga, J. Darkwa, M. Worall, W. Su, The effect of nucleating agent on the multiphase change materials for energy storage in buildings, Appl. Therm. Eng. 239 (2024) 122153, https://doi.org/10.1016/j.applthermaleng.2023.122153.

[26] W. Su, J. Darkwa, T. Zhou, D. Du, G. Kokogiannakis, Y. Li, et al., Development of composite microencapsulated phase change materials for multi-temperature thermal energy storage, Crystals (2023) 13, https://doi.org/10.3390/cryst13081167.

[27] M. Yang, Molecular dynamics simulations: chemical advances and applications, J. Phys. Conf. Ser. 2608 (2023) 4–6, https://doi.org/10.1088/1742-6596/2608/1/012044.

[28] Z. Rao, S. Wang, F. Peng, Self diffusion of the nano-encapsulated phase change materials: a molecular dynamics study, Appl. Energy 100 (2012) 303–308, https://doi.org/10.1016/j.apenergy.2012.05.022.

[29] H. Tafrishi, S. Sadeghzadeh, Molecular Dynamics Simulations of Phase Change Materials for Thermal Energy Storage: A Review, 2022, pp. 14776–14807, https://doi.org/10.1039/d2ra02183h.

[30] X. Liu, C. Lin, Z. Rao, Diffusion and thermal conductivity of the mixture of paraffin and polystyrene for thermal energy storage: a molecular dynamics study, J. Energy Inst. 90 (2017) 534–543, https://doi.org/10.1016/j.joei.2016.05.008.

[31] M. Zhang, C. Wang, A. Luo, Z. Liu, X. Zhang, Molecular dynamics simulation on thermophysics of paraffin/EVA/graphene nanocomposites as phase change materials, Appl. Therm. Eng. 166 (2020) 114639, https://doi.org/10.1016/j.applthermaleng.2019.114639.

[32] Y. Ding, M. Zhang, K.W. Shah, X. Zhang, Thermophysics of pristine and functionalized carbon nanotube reinforced paraffin/EVA composites as phase change materials: a molecular dynamics study, J. Nanopart. Res. (2022) 24, https://doi.org/10.1007/s11051-022-05457-9.

[33] R. Sinaga, J. Darkwa, S.A. Omer, M. Worall, The microencapsulation, thermal enhancement, and applications of medium and high-melting temperature phase change materials: a review, Int. J. Energy Res. (2022), https://doi.org/10.1002/er.7860.

[34] S. Chavan, V. Gumtapure, Perumal D. Arumuga, Characterization of linear low-density polyethylene with graphene as thermal energy storage material, Mater. Res. Express 2019 6, https://doi.org/10.1088/2053-1591/ab0e36.

[35] A.D. MacKerell, D. Bashford, M. Bellott, R.L. Dunbrack, J.D. Evanseck, M.J. Field, et al., All-atom empirical potential for molecular modeling and dynamics studies of proteins, J. Phys. Chem. B 102 (1998) 3586–3616, https://doi.org/10.1021/jp973084f.

[36] J. Tersoff, Carbon defects and defect reactions in silicon, Phys. Rev. Lett. 64 (1990) 1757–1760, https://doi.org/10.1103/PhysRevLett.64.1757.

[37] S. Plimpton, Fast parallel algorithms for short-range molecular dynamics, J. Comput. Phys. 117 (1995) 1–19, https://doi.org/10.1006/jcph.1995.1039.

[38] J. Delhommelle, P. Millié, Inadequacy of the Lorentz-Berthelot combining rules for accurate predictions of equilibrium properties by molecular simulation, Mol. Phys. 99 (2001) 619–625, https://doi.org/10.1080/00268970010020041.

[39] C.Y. Zhao, Y.B. Tao, Y.S. Yu, Molecular dynamics simulation of thermal and phonon transport characteristics of nanocomposite phase change material, J. Mol. Liq. (2021) 329, https://doi.org/10.1016/j.molliq.2021.115448.

[40] Z. Rao, S. Wang, M. Wu, Y. Zhang, F. Li, Molecular dynamics simulations of melting behavior of alkane as phase change material, Energ. Conver. Manage. 64 (2012) 152–156, https://doi.org/10.1016/j.enconman.2012.05.013.

[41] H. Tafrishi, S. Sadeghzadeh, F. Molaei, H. Siavoshi, Investigating the effects of adding hybrid nanoparticles, graphene and boron nitride nanosheets, to octadecane on its thermal properties, RSC Adv. 10 (2020) 14785–14793, https://doi.org/10.1039/d0ra01847c.

[42] C.Y. Zhao, Y.B. Tao, Y.S. Yu, Molecular dynamics simulation of nanoparticle effect on melting enthalpy of paraffin phase change material, Int. J. Heat Mass Transf. (2020) 150, https://doi.org/10.1016/j.ijheatmasstransfer.2020.119382.

[43] S. Chavan, V. Gumtapure, Perumal D. Arumuga, Computational investigation of bounded domain with different orientations using CPCM, J. Energy Storage 22 (2019) 355–372, https://doi.org/10.1016/j.est.2019.02.018.

[44] A. Kandelbauer, G. Wuzella, A. Mahendran, I. Taudes, P. Widsten, Model-free kinetic analysis of melamine-formaldehyde resin cure, Chem. Eng. J. 152 (2009) 556–565, https://doi.org/10.1016/j.cej.2009.05.027.

[45] S. Bône, C. Vautrin, V. Barbesant, S. Truchon, I. Harrison, C. Geffroy, Microencapsulated fragrances in melamine formaldehyde resins, Chimia (Aarau) 65 (2011) 177–181, https://doi.org/10.2533/chimia.2011.177.

[46] K. Vanommeslaeghe, E. Hatcher, C. Acharya, S. Kundu, S. Zhong, J. Shim, E. Darian, O. Guvench, P. Lopes, I.M.A.J. Vorobyov, CHARMM general force field: a force field for drug-like molecules compatible with the CHARMM all-atom additive biological force fields, J. Comput. Chem. 31 (4) (2010) 671–690, https://doi.org/10.1002/jcc.21367.

[47] C.G. Mayne, J. Saam, K. Schulten, E. Tajkhorshid, J.C. Gumbart, Rapid parameterization of small molecules using the force field toolkit, J. Comput. Chem. 34 (2013) 2757–2770, https://doi.org/10.1002/jcc.23422.

[48] F. Neese, The ORCA program system, Wiley Interdiscip. Rev. Comput. Mol. Sci. 2 (2012) 73–78, https://doi.org/10.1002/wcms.81.

[49] H. Cao, X. Cao, X. Zhao, D. Guo, Y. Liu, J. Bian, Molecular dynamics simulation of wax molecules aggregational crystallization behavior during cooling of crude oil mixture, Case Stud. Therm. Eng. 37 (2022) 102298, https://doi.org/10.1016/j.csite.2022.102298.

[50] C. Lin, Z. Rao, Thermal conductivity enhancement of paraffin by adding boron nitride nanostructures: a molecular dynamics study, Appl. Therm. Eng. 110 (2017) 1411–1419, https://doi.org/10.1016/j.applthermaleng.2016.09.065.

[51] D.J. Evans, B.L. Holian, The Nose–Hoover Thermostat 83, 1985, https://doi.org/10.1063/1.449071.

[52] M.E. Tuckerman, J. Alejandre, R. López-Rendón, A.L. Jochim, G.J. Martyna, A Liouville-operator derived measure-preserving integrator for molecular dynamics simulations in the isothermal-isobaric ensemble, J. Phys. A Math. Gen. 39 (2006) 5629–5651, https://doi.org/10.1088/0305-4470/39/19/S18.

[53] Y.W. Tang, Z. Huang, X. Wang, X.C. Zeng, Molecular dynamics simulations of thermal conductivity of silicon nanotubes, J. Comput. Theor. Nanosci. 3 (2006) 824–829, https://doi.org/10.1166/jctn.2006.023.

[54] C. Vélez, J.M. Ortiz De Zárate, M. Khayet, Thermal properties of n-pentadecane, n-heptadecane and n-nonadecane in the solid/liquid phase change region, Int. J. Therm. Sci. 94 (2015) 139–146, https://doi.org/10.1016/j.ijthermalsci.2015.03.001.